Purdue University

# Purdue e-Pubs

Open Access Theses                                                      Theses and Dissertations

5-2018

# Enrichment of Turbulence Field Using Wavelets

Yifan Du
*Purdue University*

Follow this and additional works at: https://docs.lib.purdue.edu/open_access_theses

ENRICHMENT OF TURBULENCE FIELD USING WAVELETS

A Thesis

Submitted to the Faculty

of

Purdue University

by

Yifan Du

In Partial Fulfillment of the

Requirements for the Degree

of

Master of Science

May 2018

Purdue University

West Lafayette, Indiana

# THE PURDUE UNIVERSITY GRADUATE SCHOOL
# STATEMENT OF THESIS APPROVAL

Dr. Guang Lin, Chair

School of Mechanical Engineering

Dr. Ivan C. Christov

School of Mechanical Engineering

Dr. Carlo Scalo

School of Mechanical Engineering

**Approved by:**

Dr. Jay P. Gore

Director Of Graduate Programs

## ACKNOWLEDGMENTS

I would first like to thank my thesis advisor Prof. Guang Lin of the Mechanical Engineering Department at Purdue University for the continuous support of my Ph.D study and research, for his patience, motivation, enthusiasm, and immense knowledge. His guidance helped me in all the time of research and writing of this thesis. I could not have imagined having a better advisor and mentor for my Ph.D study.

I would also like to thank Dr. Wen Huang at Rice University who was involved in the implementation and validation of my model. Without his passionate and patient participation, the project could not have been successfully conducted.

I would also like to acknowledge Prof. Ivan Christov of the Mechanical Engineering at Purdue University as the second reader of this thesis, and I am gratefully thankful for his very valuable comments on this thesis.

Finally, I must express my very profound gratitude to my parents and to my partner for providing me with unfailing support and continuous encouragement throughout my years of study and through the process of researching and writing this thesis. This accomplishment would not have been possible without them. Thank you.

TABLE OF CONTENTS

## LIST OF TABLES

## LIST OF FIGURES

# SYMBOLS

| | |
|---|---|
| $\boldsymbol{u}$ | velocity vector |
| $u, v, w$ | velocity components |
| $\langle \boldsymbol{u} \rangle$ | ensemble average of $\boldsymbol{u}$ |
| $P$ | equivalent pressure, $P = \frac{p}{\rho}$ |
| $\otimes$ | tensor product |
| $\times$ | Cartesian product |
| $\odot$ | Hadamard product |
| $\nabla \cdot \boldsymbol{u}$ | divergence of $\boldsymbol{u}$ |
| $\nabla \times \boldsymbol{u}$ | curl of $\boldsymbol{u}$ |
| $\mathbb{R}$ | real number space |
| $\mathbb{Z}$ | integer number space |
| $L^2$ | Lebesgue spaces with index $p = 2$ |
| $|\Omega|$ | Volume of region $\Omega$ |
| $(V_j)_{j \in \mathbb{Z}}$ | MRA space |
| $\phi(x)$ | scaling function of a 1-D MRA |
| $\psi(x)$ | wavelet function of a 1-D MRA |
| $\mathscr{F}\{\psi\}$ | Fourier transform of function $\psi$ |
| $\tilde{\boldsymbol{u}}$ | velocity $\boldsymbol{u}$ filtered with some filter |
| $G * \boldsymbol{u}$ | u convoluted with $G$ |
| $\widehat{\boldsymbol{u}}$ | 3-D Fourier Transform of $\boldsymbol{u}$ |
| $\check{\boldsymbol{u}}$ | 3-D inverse Fourier Transform of $\boldsymbol{u}$ |
| $\mathbf{F}$ | Fourier transform matrix |
| $\mathbf{B}^*$ | complex conjugate transpose of matrix $\mathbf{B}$ |
| $\overline{\mathbf{B}}$ | complex conjugate of matrix $\mathbf{B}$ |
| $\mathbf{B}^{-1}$ | inverse of matrix $\mathbf{B}$ |

$\mathcal{N}$   total space (a vector space)

$\mathcal{Q}$   quotient manifold

$T_x\mathcal{M}$   tangent space of manifold $\mathcal{M}$ at point $x$

$T\mathcal{M}$   tangent bundle of manifold $\mathcal{M}$

$\eta_x, \xi_x, \zeta_x$   tangent vectors

$\mathrm{D}f(x)[\eta_x]$   directional derivative of $f(x)$ on tangent vector $\eta_x$

$\mathrm{grad}\, f$   Riemannian gradient of $f$

# ABBREVIATIONS

| | |
|------|------------------------------------|
| SRFM | Synthetic Random Fourier Method |
| DNS | Direct Numerical Simulation |
| LES | Large Eddy Simulation |
| RANS | Reynold's Averaged Navier Stokes |
| HIT | Homogeneous Isotropic Turbulence |
| MRA | Multiresolution Analysis |
| FWT | Fast Wavelet Transform |
| FFT | Fast Fourier Transform |
| DFT | Discrete Wavelet Transform |
| TKE | Turbulent Kinetic Energy |

ABSTRACT

Du, Yifan MS, Purdue University, May 2018. Enrichment of Turbulence Field Using Wavelets. Major Professor: Guang Lin, School of Mechanical Engineering.

This thesis is composed of two parts. The first part presents a new turbulence generation method based on stochastic wavelets and tests various properties of the generated turbulence field in both the homogeneous and inhomogeneous cases. Numerical results indicate that turbulence fields can be generated with much smaller bases in comparison to synthetic Fourier methods while maintaining comparable accuracy. Adaptive generation of inhomogeneous turbulence is achieved by a scale reduction algorithm, which greatly reduces the computational cost and practically introduces no error. The generating formula proposed in this research could be adjusted to generate fully inhomogeneous and anisotropic turbulence with given RANS data under a divergence-free constraint, which was not achieved previously in similar research. Numerical examples show that the generated homogeneous and inhomogeneous turbulence are in good agreement with the input data and theoretical results.

The second part presents a framework of solving turbulence deconvolution problems using optimization techniques on Riemannian manifolds. A filtered velocity field was deconvoluted without any information of the filter. The deconvolution results shows high accuracy compared with the original velocity field. The computational cost of the optimization problem was largely reduced using wavelet representation while still maintaining high accuracy. Utilization of divergence-free wavelets ensures the incompressible property of deconvolution results, which was barely achieved in previous research.

# Part I

# Introduction

## 1. INTRODUCTION

Turbulence is one of the most important and complex phenomena in classical fluid mechanics, which has been an important research topic for more than a hundred years. Due to its multiscale and nonlinear nature (Sagaut et al. [2013]), turbulence is extremely difficult to understand. Although the flow pattern is complex, incompressible turbulence is still governed by the Navier-Stokes equation:

$$\nabla \cdot \boldsymbol{u} = 0, \tag{1.1}$$

$$\frac{\partial \boldsymbol{u}}{\partial t} + \nabla \cdot (\boldsymbol{u} \otimes \boldsymbol{u}) = -\nabla P + \frac{1}{\mathrm{Re}} \Delta \boldsymbol{u}. \tag{1.2}$$

This system could be directly discretized and solved using various numerical methods. However, the computational cost of DNS is too large for pratical engineering problems. Kolmogorov scale of turbulent flow is defined as follow (Kolmogorov [1941]):

$$\eta = \left( \frac{\nu^3}{\epsilon} \right)^{\frac{1}{4}}.$$

Direct Numerical Simulation must resolve all scales larger that $\eta$, thus grid size of DNS must be smaller than $\eta$. Also, the integral scale of turbulent flow must be smaller than the domain size. Combining all conditions above, the following estimation was made:

$$N^3 \geqslant \mathrm{Re}_\eta^{\frac{9}{4}},$$

in which $N^3$ is the total number of mesh grids. Computation of such cost is nearly impossible to conduct in engineering problems. In late 20th century, a class of models were proposed to predict the behaviors of turbulent flow for aeronautic and astronautic applications, which are well known as turbulence models (Pope [2001]). Turbulence models are dedicated to close RANS equations and give a prediction of statistical quantities of turbulence field, including mean and covariance of velocity

field. Although in some cases turbulence models show deficiency, they give a good approximation of turbulence statistics distribution in many situations.

At the same time, a type of simulation techniques arose that could correctly predict dynamics of turbulent flow while largely reducing computational cost compared to DNS, which is called Large Eddy Simulation. In LES, (1.1) and (1.2) are filtered to discard all scales smaller than the filter width $\delta$:

$$\nabla \cdot \tilde{\boldsymbol{u}} = 0, \tag{1.3}$$

$$\frac{\partial \tilde{\boldsymbol{u}}}{\partial t} + \nabla \cdot (\tilde{\boldsymbol{u}} \otimes \tilde{\boldsymbol{u}}) = -\nabla \tilde{P} + \frac{1}{\text{Re}}\Delta \tilde{\boldsymbol{u}} - \boldsymbol{T}, \tag{1.4}$$

where $\boldsymbol{T}$ is subgrid stress, which is closed by a subgrid model:

$$\boldsymbol{T} = F(\delta, \nabla \boldsymbol{u}). \tag{1.5}$$

In this research, super-resolution is achieved from RANS data and LES data (filtered DNS data) using wavelets. In part II, a fluctuation field is generated from RANS data using stochastic wavelets, the statistics of which coincide with RANS data. In part III, a filtered turbulent velocity field is deconvoluted to find unfiltered velocity field using wavelet representation along with optimization techniques on Riemannian manifold.

## 1.1    Turbulence generation techniques

Turbulence generation has been an important research topic in fluid mechanics area for decades. Before wide application of Direct Numerical Simulation (DNS) and Large Eddy Simulation (LES) in fundamental turbulence research, explicit synthesis scheme was constructed to study turbulence related phenomenon. Kraichnan [1970] proposed a divergence-free synthesis method using random Fourier series expansion and applied it on diffusion and particle dispersion in Homogeneous Isotropic Turbulence (HIT). Subsequent improvement and modification soon turned it into a viable tool for both theoretical research and acoustic related computation (Juves [1999],

Fung et al. [1992]). With the increase of computational power, DNS and LES became realistic and successfully enabled scientists to acquire knowledge from more complex flow phenomenon (Rogallo and Moin [1984], Moin and Mahesh [1998]). Meanwhile, turbulence generation techniques were gradually modified to generate high-fidelity inlet boundary conditions for DNS and LES, as well as interface generation in Detached Eddy Simulation (Spalart [2009]), rather than directly used for turbulent flow prediction. Synthetic Random Fourier Method (SRFM) has become one of the most important methods for inflow turbulence generation. However, despite its wide application in turbulence related research, SRFM suffers several drawbacks. Fourier basis is naturally not proper for representation of inhomogeneous turbulence because of its global properties. Although Le et al. [1997] proposed a transform to map isotropic homogeneous turbulence generated from SRFM to general turbulence field with any given Reynolds stress, the transformed turbulence field is no longer incompressible (Wu [2017]). Also, SRFM uses global Fourier basis for all wavenumbers, which lead to very large computational cost.

In the meantime, wavelet noise tool was gradually developed for fluid simulation in computer graphics area and the movie industry. Perlin [1985] constructed the widely used turbulence function that could describe band-limited noise. The form of Perlin noise was very close to a series of random wavelets. Cook and DeRose [2005] rigorously constructed band-limited wavelet noise upsampling and downsampling procedure. Bridson et al. [2007] used Perlin noise as vector potential to generate an incompressible flow field. Kim et al. [2008] constructed high-resolution incompressible flow fields based on the wavelet noise of Cook and DeRose [2005]. As a new mathematical tool developed in 1980s, wavelet exhibits many delicate and fine properties. Similar to Fourier series, wavelet series can be complete basis for $\mathbb{L}^2$ function space. Unlike Fourier transform which can only extract global frequency (wavenumber) information from functions, wavelet transform can contain both frequency (wavenumber) and location information, which is an appropriate tool for inhomogeneous turbulence (Farge [1992]).

In this research, a turbulence generation method based on stochastic wavelets is developed and tested in both homogeneous and inhomogeneous cases. Turbulence generation method is proposed in Sec. 2, including generation system, boundary condition treatment, input spectrum and scale reduction algorithm. Numerical results are presented in Sec. 3 for both isotropic homogeneous turbulence and fully developed channel flow to validate its accuracy. An comprehensive discussion and analysis of the proposed method is made in Sec. 9. An proof of Reynolds stress preservation of this method is presented in Sec. A.

## 1.2   Subfilter enrichment and deconvolution techniques

Accurate prediction of space-time correlation in subgrid modeling is vital for Large Eddy Simulations of various high Reynolds number flow in industrial and enviromental applications (He et al. [2017], Ghate and Lele [2017]). Much of previous research focus on explicit evaluation of subgrid structure using existing theories on energy spectrum and various types of modes. Such type of kinematic simulation was first introduced by Fung et al. [1992], in which a series of random Fourier modes equipped with certain energy distribution in wavenumber and frequency space were used to synthesize dynamic homogeneous isotropic turbulence. In the following research on this approach (Juves [1999], Smirnov et al. [2001], Castro and Paz [2013]), subgrid vortices and structures of Large Eddy Simulation could be accurately reconstructed in isotropic homogeneous turbulence. In a recent paper, Ghate and Lele [2017] proposed to explicitly synthesize subgrid scales of LES result of planetary boundary layer using Fourier-Gabor modes. Although the reconstruction results coincide well with DNS data of the same configuration, this method suffers several drawbacks. Some theoretical results in plantary boundary layer and homogeneous shear flow were applied in the methedology, which largely undermines its generality in different situation of turbulent flow. Also, Fourier-Gabor modes cannot maintain no-penetration condition at boundary, thus additional Laplace equation need to be solved and superimposed on

synthetic results, which increases the complexity of this procedure. Till now kinematic simulation is incapable of subgrid enrichment on LES result of general inhomogeneous turbulence.

Another approach of reconstruction of subgrid fluctuation is using various deconvolution techniques. The results of Large Eddy Simulation can be treated as filtered DNS results with error introduced by subgrid model. Scotti and Meneveau [1999] used fractal interpolation methods to synthesize subgrid flctuations of turbulent flow. Domaradzki and Loh [1999] evaluated subgrid quantities using an approximate inverse filter. Compared to kinematic simulation, blind deconvolution methods are more general for different flow situation since there is no need for prior knowledge of subgrid structure, which is difficult to acquire in complex turbulent flow.

In recent years, numerous algorithms have been proposed to solve blind deconvolution problems in image and signal processing area (Ayers and Dainty [1988], Katsaggelos and Lay [1991], Kundur and Hatzinakos [1996], Levin et al. [2009]). Theoretically, blind deconvolution problem is equivalent to an optimization problem on certain complex vector space. Recently, a framework of solving blind deconvolution problem using optimization techniques on Riemannian manifold was proposed, which could successfully recover blurred image under proper condition (Huang and Hand [2017]). However, information contained turbulent flow field is different from natural image since multiscale hierarchy of turbulent flow brings more difficulty to optimization proccedure. Also, divergence-free should be maintained during optimization process for mass conservation. Proper vector space need to be find in order to correctly represent multiscale structure of turbulence.

Wavelet is a type of mathematical tool widely used in image and signal processing area (Gomes and Velho [2015], Mallat [1999]). It was introduced into turbulence related area as a proper tool for representations and diagnoses of turbulence field (Farge [1992], Meneveau [1991]). Divergence-free and curl-free wavelets were constructed by Deriaz and Perrier [2009] to conduct orthogonal Helmholtz decomposition of vector field using wavelets. In Deriaz and Perrier [2006] such wavelets were used to analyze

compressible and incompressible turbulence fields. Data of incompressible turbulent flow is sparse under a divergence-free wavelet representation, thus the dimension of the optimization problem can be significantly reduced. Also, a divergence free wavelet basis ensures mass conservation along optimization procedure. Thus, wavelet theory offers a proper space in which the optimization is conducted.

# Part II

# Turbulence Generation using Stochastic Wavelet Model

## 2. METHODOLOGY

### 2.1  Turbulence Generation Process

### 2.1.1  Generation of static turbulence field

The model presented in this work allows to generate inhomogeneous stochastic turbulent velocity field based on RANS data. Many previous research (Shur et al. [2014], Lund et al. [1998]) suggested that the fluctuation velocity field could be expressed in the following form:

$$\boldsymbol{u} = \boldsymbol{A} \cdot (\nabla \times \boldsymbol{M}), \tag{2.1}$$

where $\boldsymbol{u} = (u, v, w)$ is the fluctuation velocity. $\boldsymbol{u}$ is constructed in the manner of equation Eq.(2.1) so that corresponding second order momentum $\langle \boldsymbol{u}\boldsymbol{u} \rangle$ is equal to Reynolds stress tensor. $\boldsymbol{A}(x)$ is the Cholesky decomposition of Reynolds stress tensor $\boldsymbol{R}(x)$ (Jarrin et al. [2009], Shur et al. [2014]) :

$$\boldsymbol{R} = \boldsymbol{A}^T \boldsymbol{A}, \tag{2.2}$$

where $\boldsymbol{A}^T$ denotes the transpose of $\boldsymbol{A}$. $\boldsymbol{M} = (M_x, M_y, M_z)$ is vector potential field. $\nabla \times \boldsymbol{M}$ term is constructed to be divergence free as suggested in Shur et al. [2014]. In Kim et al. [2008], vector potential field was constructed using wavelet noise in Cook and DeRose [2005]. Similarly $\boldsymbol{M}$ is decomposed into a sum of wavelet modes:

$$\boldsymbol{M}(\boldsymbol{x}) = \sum_{|\boldsymbol{k}| \in K} \sum_{\boldsymbol{x}_p}^{N_i} q_{\boldsymbol{x}_p, \boldsymbol{k}} \, \boldsymbol{O}_{\boldsymbol{x}_p, \boldsymbol{k}}(\omega_{\boldsymbol{x}_p, \boldsymbol{k}} \Psi_{\boldsymbol{k}}(\boldsymbol{x} - \boldsymbol{x}_p)), \tag{2.3}$$

where $\boldsymbol{x}_p = (x_p, y_p, z_p)$ is the position of wavelet basis in physical space. $\boldsymbol{k} = (k_x, k_y, k_z)$ is wavenumber of the wavelet basis. Definition of such wavenumber is according to Perrier et al. [1995]. $K = \{l_1, l_2, ..., l_M\}$ is a series of magnitude of wavenumber vector. For each $l_i$, $\boldsymbol{k}$ is randomly chosen on a sphere of radius $l_i$ in

spectral space. Such a construction coincides with the nature of energy spectrum function, i.e. $E(l)$ is turbulent kinetic energy distributed on a sphere of radius $l$ in spectral space. $\boldsymbol{x}_p$ is the location of $N_i$ randomly distributed wavelets. The number $N_i$ for each wavenumber $l_i$ is determined using the following expression deducted from uniformly distributed wavelets:

$$N_i = \left[ |\Omega| \left( \frac{l_i}{k_0} \right)^3 \right],$$
(2.4)

where $\Omega$ represents the flow domain. $\omega_{\boldsymbol{x}_p,b} = (\omega^1_{\boldsymbol{x}_p,b}, \omega^2_{\boldsymbol{x}_p,b}, \omega^3_{\boldsymbol{x}_p,b})$ is a random vector series assumed to be normally distributed with the following statistics:

$$\langle \omega^i_{\boldsymbol{x}_p,\boldsymbol{k}} \rangle = 0,$$
(2.5)

$$\langle \omega^i_{\boldsymbol{x}_p,\boldsymbol{k}} \omega^j_{\mathbf{x}_p,\boldsymbol{k}} \rangle = \delta_{ij}.$$
(2.6)

$\Psi(\boldsymbol{x})$ is 3D wavelet basis function constructed in the following tensor-product way:

$$\Psi_{\boldsymbol{k}}(\boldsymbol{x} - \boldsymbol{x}_p) = \psi \left( \frac{k_x}{k_0} (x - x_p) \right) \psi \left( \frac{k_y}{k_0} (y - y_p) \right) \psi \left( \frac{k_z}{k_0} (z - z_p) \right).$$
(2.7)

From the analytical result in Deriaz and Perrier [2005], $\Psi_{\boldsymbol{k}}(\boldsymbol{x} - \boldsymbol{x}_p)$ in the above form might not be a complete basis of $\mathbb{L}^2(\mathbb{R}^3)$. However, the basis function above is chosen because of its localization in both physical and spectral space, which offers an appropriate tool for description and synthesis of turbulence (Farge [1992]). Wavelet function of enough high order cancellation is chosen as 1-D wavelet function $\psi(\cdot)$:

$$\int_{\mathbb{R}} x^p \psi(x) \, \mathrm{d}x,$$
(2.8)

in which $p$ is the order of cancellation. As stated in Farge [1992] and Perrier et al. [1995], the wavelet spectrum of a function approximates its Fourier spectrum at high frequency (wavenumber) as long as the wavelet function has enough high order cancellation. $k_0$ is the Fourier wavenumber of wavelet function where its Fourier spectrum reaches peak, i.e.:

$$\mathscr{F}\{\psi(x)\}(k_0) = \max_{k \in \mathbb{R}} \mathscr{F}\{\psi(x)\}(k).$$
(2.9)

The wavelet function $\psi(x)$ is localized in both physical and spectral space, which represents a local structure of turbulent field with certain band width of wavenumber. $k_0$ defined in Eq.(2.9) characterizes the most energetic wavenumber of such structure. $\boldsymbol{O}$ in Eq.(2.3) is a random rotation matrix in 3-dimensional space, i.e. $\boldsymbol{O} \in SO(3)$. An efficient way of generating uniformly distributed random rotation is from Stuelpnagel [1964], where random rotation matrix is generated from random quaternion:

$$\boldsymbol{O} = \begin{pmatrix} 1 - 2c_u^2 - 2d_u^2 & 2b_u c_u - 2a_u d_u & 2b_u d_u + 2a_u c_u \\ 2b_u c_u + 2a_u d_u & 1 - 2b_u^2 - 2d_u^2 & 2c_u d_u - 2a_u b_u \\ 2b_u d_u - 2a_u c_u & 2c_u d_u + 2a_u b_u & 1 - 2b_u^2 - 2c_u^2 \end{pmatrix},$$

where $a_u$, $b_u$, $c_u$, $d_u$ are components of a unit quaterion:

$$a_u = \frac{a}{|\boldsymbol{q}|}, b_u = \frac{b}{|\boldsymbol{q}|}, c_u = \frac{c}{|\boldsymbol{q}|}, d_u = \frac{d}{|\boldsymbol{q}|},$$

where $\boldsymbol{q} = a + b\boldsymbol{i} + c\boldsymbol{j} + d\boldsymbol{k}$ is a random quaterion with $a, b, c, d \sim N(0, 1)$.

$q_{\boldsymbol{x}_p, \boldsymbol{k}}$ is a series of normalized weights to maintain local spectrum property of RANS data:

$$q_{\boldsymbol{x}_p, \boldsymbol{k}} = \sqrt{\frac{E(l)\Delta l}{2k_t c_l}}, \tag{2.10}$$

in which $E(l)$ represents local energy spectrum, which is a known function used as input. Various of different spectrum can be used as input spectrum to characterize multiscale feature of turbulence field. $\Delta l$ is difference between two neighboring wavenumber magnitudes in $K$ in Eq.(2.3). $k_t$ is the turbulent kinetic energy with the following relation:

$$k_t = \int_0^\infty E(l)\, dl. \tag{2.11}$$

$c_l$ is a coefficient determined using Monte Carlo method:

$$c_l = \frac{N_i}{|\Omega|} \left\langle \int_S \frac{\partial}{\partial x} \Psi_{\boldsymbol{k}}\, dV \right\rangle = \frac{N_i}{|\Omega|} \left\langle \int_S \frac{\partial}{\partial y} \Psi_{\boldsymbol{k}}\, dV \right\rangle = \frac{N_i}{|\Omega|} \left\langle \int_S \frac{\partial}{\partial z} \Psi_{\boldsymbol{k}}\, dV \right\rangle, \tag{2.12}$$

where the ensemble average$\langle \cdot \rangle$ is performed on random variable $\boldsymbol{k}$. Such ensemble average diverges without restriction on $\boldsymbol{k}$. In real flow problems, flow domain with finite size can only contain wavelet modes with finite large support, which prevents any

component of $\boldsymbol{k}$ approaching zero and removes singularity in Eq.(2.12). $S = \text{supp}(\Psi_{\boldsymbol{k}})$ is the support set of tensor-product basis function. It should be noted that depending on the choice of wavelet basis $\psi(\cdot)$, $\Psi_{\boldsymbol{k}}$ may not be compactly supported, in which case $S$ is the effective support set of function $\Psi_{\boldsymbol{k}}$ in numerical sense, which could be defined as follow:

$$S = \{(\boldsymbol{x}, t) | |\Psi_{\boldsymbol{k}}(\boldsymbol{x}, t)| < \delta\}, \tag{2.13}$$

where $\delta$ is a small positive number.

Construction of such system including Eq.(2.1), (2.2), (2.3), (2.4), (2.7), (2.10) coincides with the multi-scale and inhomogeneous nature of turbulence, which needs further explanation. It has been stated clearly in multiple literatures that wavelets are good tools for performing energy decomposition to find possible atoms in physical-spectral space (Farge [1992], Farge and Schneider [2001]). In Eq.(2.3) velocity vector potential $\boldsymbol{M}$ is decomposed into a series of wavelet basis $\Psi_{\boldsymbol{k}}(\boldsymbol{x} - \boldsymbol{x}_p)$ with its own characteristic wavenumber $\boldsymbol{k}$ and position $\boldsymbol{x}_p$. Each wavelet mode represents a vortex structure localized both around position $\boldsymbol{x}_p$ in physical space and wavenumber $\boldsymbol{k}$ in spectral space. Each $\Psi_{\boldsymbol{k}}(\boldsymbol{x} - \boldsymbol{x}_p)$ is equipped with a random rotation matrix $\boldsymbol{O}_{\boldsymbol{x}_p, \boldsymbol{k}}$ to make sure Eq.2.3 is invariant under rotation. Summation on position $\boldsymbol{x}_p$ indicates a layer of vortices with same magnitude of characteristic wavenumber at different position. The whole fluctuation velocity field is a superposition of layers of local structures with different magnitudes of wavenumbers. The preservation of Reynolds stress tensor in the construction of Eq.(2.1), (2.2), (2.3) is in Appendix.

Such construction of fluctuation velocity field resembles the Synthetic Eddy Methods (SEM) used to generate inlet flow conditions of LES in previous researchs (Jarrin et al. [2009], Poletto et al. [2013], etc.). However, unlike wavelet functions used in this research, the spectral and physical space properties of functions used to generate structures of different scales in SEM remain unknown. Also, numbers of modes with different scales used in eddy synthesis often need to be determined by experience and tests. Eq.(2.4) gives a quantitative representation of number of wavelet modes in this system, which comes from the density of wavelets used to completely cover each scale

in wavelet theory (Hernández and Weiss [1996], Deriaz and Perrier [2005]). Intuitively speaking, Eq.(2.4) indicates that turbulence field with larger size need more wavelet modes to cover. Also, there are more small-scale structures with higher wavenumber than large scales structures with lower wavenumber.

Many previous research have constructed multi-scale system of turbulence using Fourier basis (Fung et al. [1992], Juves [1999]), and successfully simulated isotropic homogeneous turbulence from it. However, in general cases of anisotropic inhomogeneous turbulence, such construction encounters serious problems. Fourier basis is global in the whole turbulence field, thus the construction procedure in Fung et al. [1992] is not applicable for generation of turbulence with anisotropy and inhomogeneity. Billson et al. [2003], Shur et al. [2014] modified Fourier based reconstruction system so that it could be used to generate inhomogeneous turbulence by multiplying each Fourier basis with a weighing function which quantifies the distribution of turbulent kinetic energy on each scale locally. However, such modification changes the properties of Fourier basis and causes aliasing between different wavenumbers. In this research, this problem is solved by using random wavelets, which are local in both spectral space and physical space rather than random Fourier basis.

### 2.1.2   Generation of dynamic turbulence field

For high Reynolds number turbulence, structures of large and small scales might behave differently according to their own kinematic and dynamic properties, thus need to be dealt with differently (Pope [2001], Fung et al. [1992], Lafitte et al. [2014]). Large scale contains most of turbulent kinetic energy of the whole turbulence field, while small scale include inertial subrange and viscous subrange. The separation of large and small scales can be achieved by introducing a cutoff wavenumber $k_c$. However, previous research on turbulence generation indicates that such $k_c$ might be difficult to determine a priori. Here $k_c$ is determined with the following relation:

$$k_c = 2k_e, \tag{2.14}$$

where $k_e$ is the wavenumber where maximum energy spectrum occurs. The magnitudes of wavenumber in $K$ in Eq.(2.3) can be separated into large scales and small scales. For large scales, time advance is achieved by advection induced by mean velocity field $\boldsymbol{U}$ computed from RANS model and a random Gaussian advective velocity $\boldsymbol{W}_{\boldsymbol{k}}$ (Fung et al. [1992], Poletto et al. [2013]):

$$\boldsymbol{x}_p(t) = \boldsymbol{x}_0 + \int_0^{t'} \boldsymbol{U}(t') + \boldsymbol{W}_{\boldsymbol{k}}(t')\, \mathrm{d}t', \qquad (2.15)$$

where $\boldsymbol{x}_0$ is initial position of a large scale mode. It is reasonable to assume that $\boldsymbol{W}_{\boldsymbol{k}}$ has zero mean and variance equal to that of velocity field of mode $\boldsymbol{k}$:

$$\langle \boldsymbol{W}_{i,\boldsymbol{k}}^2 \rangle = \frac{E(l)\Delta l}{2k_t} \langle u_i u_i \rangle, \qquad (2.16)$$

where $l = |\boldsymbol{k}|$, $i = 1, 2, 3$ represents three space coordinates and does not imply summation on repeated index.

For small scales structures, Fung et al. [1992] and Lafitte et al. [2014] suggest that small scales vortices are advected by large scale structures and mean velocity field. A similar formula as Eq.(2.16) can be written as follow:

$$\boldsymbol{x}_p(t) = \boldsymbol{x}_0 + \int_0^{t'} \boldsymbol{U}(t') + \boldsymbol{u}_l(t')\, \mathrm{d}t', \qquad (2.17)$$

where $\boldsymbol{u}_l$ means large scale velocity field. For small scale basis, Eq.(2.1), (2.2), (2.3) still hold. However, to predict right Lagrangian decorrelation process, basis function $\Psi_{\boldsymbol{x}_p,\boldsymbol{k}}$ is modified to the following shape:

$$\Psi_{\boldsymbol{k}}(\boldsymbol{x} - \boldsymbol{x}_p, t) = \psi\left(\frac{k_x}{k_0}(x - x_p)\right) \psi\left(\frac{k_y}{k_0}(y - y_p)\right) \psi\left(\frac{k_z}{k_0}(z - z_p)\right) \psi\left(\frac{\omega_{\boldsymbol{k}}}{k_0}t - \phi_p\right), \qquad (2.18)$$

where $\phi_p$ is a random phase, randomly distributed in support set of function $\psi(\frac{\omega_{\boldsymbol{k}}}{k_0}t)$ with uniform distribution. $\omega_{\boldsymbol{k}}$ is a time frequency related to wavenumber $\boldsymbol{k}$. Generally structure with small wavenumber varies in a slow frequency and vice versa. In the inertial subrange, it is assumed that energy at each wavenumber $\boldsymbol{k}$ is spread over a range of frequency around a characteristic frequency related to characteristic

wavenumber. Thus here for each characteristic wavenumber $\boldsymbol{k}$ a random frequency $\omega_{\boldsymbol{k}}$ is generated with the following distribution:

$$f_\omega = \frac{1}{\sqrt{2\pi}\sigma_\omega(\boldsymbol{k})}\, \mathrm{e}^{\frac{-(\omega-\varpi(\boldsymbol{k}))^2}{2\sigma_\omega^2(\boldsymbol{k})}}, \tag{2.19}$$

where $\sigma_\omega(\boldsymbol{k}) = \varpi(\boldsymbol{k}) = \epsilon^{\frac{1}{3}}|\boldsymbol{k}|^{\frac{2}{3}}$ are variance and mean of random frequency $\omega_{\boldsymbol{k}}$(Leslie and Leith [1975]).

### 2.1.3 Incompressibility condition modification

The system Eq.2.1, 2.2, 2.3, 2.10 does not satisfy incompressible condition as the result of transformation Eq.2.1. Previous Synthetic Random Fourier Methods (SRFM) all suffer this problem. Some modified SRFM could unify divergence-free constraint, anisotropy and inhomogeneity, but they often involve some special parameter, which largely undermines their generality (Wu [2017], Smirnov et al. [2001], Huang et al. [2010], Castro and Paz [2013], Yu and Bai [2014]). A slight modification of formulas allows to generate inhomogeneous turbulence field which satisfies divergence-free constraint. The modified formulas are as follow:

$$\boldsymbol{u} = \nabla \times \boldsymbol{M}, \tag{2.20}$$

$$\boldsymbol{M}(\boldsymbol{x}) = \sum_{|\boldsymbol{k}|\in K}\sum_{\boldsymbol{x}_p}^{N_i} q_{\boldsymbol{x}_p,\boldsymbol{k}}\,\boldsymbol{O}_{\boldsymbol{x}_p,\boldsymbol{k}}(\omega_{\boldsymbol{x}_p,\boldsymbol{k}}\Psi_{\boldsymbol{k}}(\boldsymbol{x} - \boldsymbol{x}_p)), \tag{2.21}$$

$$q_{\boldsymbol{x}_p,\boldsymbol{k}} = \sqrt{\frac{E(l)\Delta l}{2c_l}}, \tag{2.22}$$

$$\langle \omega_{\boldsymbol{x}_p,\boldsymbol{k}}^i \rangle = 0, \tag{2.23}$$

$$\langle \omega_{\boldsymbol{x}_p,\boldsymbol{k}}^i \omega_{\boldsymbol{x}_p,\boldsymbol{k}}^j \rangle = \frac{3}{2}\frac{k_t(\boldsymbol{x}_p) - \delta_{ij}R_{ij}}{k_t(\boldsymbol{x}_p)}. \tag{2.24}$$

The system Eq.(2.20) to (2.24) is incompressible. Also, it considers the inhomogeneity and isotropy of turbulence field. However, this construction does not preserve full Reynolds stress, only preserves normal Reynolds stress distribution.

## 2.2  Boundary Conditions



(a) Periodic Boundary  (b) No-slip Boundary
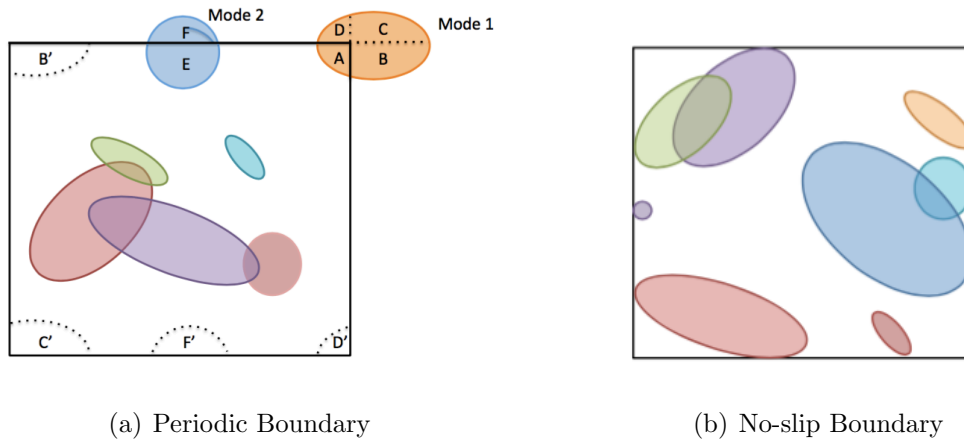
Figure 2.1.  Boundary Conditions: (a) and (b) respectively shows treatment on periodic and no-slip boundaries. In (a), circles in the plot are supports of different modes. Mode 1 is separated into $A$, $B$, $C$, $D$ parts across boundary. $A$ stays at its location and $B$, $C$, $D$ are shifted to opposite sides ($B'$, $C'$, $D'$). Mode 2 is separated into $E$, $F$ parts across boundary. $E$ stays at its location and $F'$ is shifted to opposite sides ($F'$). In (b), supports of modes are restricted in the domain so that velocities are exactly 0 on boundary.

For a large enough flow domain, boundary condition for such turbulence generation has no influence on the inner regions away from boundary. However, in order to retain flow properties near boundary, modes near boundary need to be treated differently. For periodic boundaries (Fig.2.1(a)), modes on boundary are separated into different parts and added to opposite boundaries. Such treatment maintains exact same velocity value on opposite boundaries.

For no-slip boundaries, modes are restricted to inner side of boundary (Fig.2.1(b)). In this way velocity and second-order moments on the boundary are exact zero. Also, characteristic length of modes near solid boundary is strictly restricted by its distance from boundary, which automatically creates a damping effect near boundaries.

## 2.3 Input Spectrum

### 2.3.1 Isotropic case

For high Reynolds number turbulence, homogeneous isotropic hypothesis is assumed to hold locally. Thus von Karman-Pao spectrum can be used to obtain spectral information of turbulence field. The von Karman-Pao spectrum is given by (Juves [1999], Saad et al. [2016]):

$$E(k) = \alpha \frac{u'^2}{k_e} \frac{(k/k_e)^4}{[1 + (k/k_e)^2]^{17/6}} \exp\left[ -2\left(\frac{k}{k_\eta}\right)^2 \right], \tag{2.25}$$

where $k_\eta = \epsilon^{1/4}\nu^{-3/4}$ is Kolmogorov length scale corresponding to viscous dissipation lengthscale. $\epsilon$ is turbulence dissipation rate from RANS data. $\alpha$ is determined from normalization of Eq.(2.11):

$$\alpha = \frac{55}{9\sqrt{\pi}} \frac{\Gamma(\frac{5}{6})}{\Gamma(\frac{1}{3})} \approx 1.453. \tag{2.26}$$

$k_e$ is the wavenumber related to most energetic eddies, could be determined by:

$$k_e = \sqrt{\pi} \frac{\Gamma(\frac{5}{6})}{\Gamma(\frac{1}{3})} \frac{1}{L} \approx \frac{0.746834}{L}. \tag{2.27}$$

$L = u'^3/\epsilon$ is integral lengthscale which could be computed from RANS data.

### 2.3.2 Wall turbulence case

Eq.(2.21) defines a wavenumber $k_e$ related to the energy containing structures, which could lead to a length scale $l_e$ related to $k_e$:

$$l_e = \frac{2\pi}{k_e}$$

$l_e$ corresponds to the size of most energetic eddies. In regions near wall, $l_e$ should not be larger that double the distance to the wall (Shur et al. [2014]):

$$l_e \leqslant 2d_w,$$

where $d_w$ is the distance to wall. In regions far away from wall where damping effect is not important, expression of $k_e$ returns to isotropic von-Karman spectrum. Thus a modified expression of $k_e$ considering wall effect is as follow:

$$k_e = \max\left(\sqrt{\pi}\frac{\Gamma(\frac{5}{6})}{\Gamma(\frac{1}{3})}\frac{1}{L}, \frac{\pi}{d_w}\right).$$

### 2.3.3 Spatial-Spectral decomposition

Eq.(2.3) gives a decomposition of velocity potential field in both physical and spectral space, which allows a large reduction of computational cost of reconstruction of turbulence field, especially for anisotropic inhomogeneous turbulence. Consider a fully developed channel flow the simulation result of which is shown in Sec. 3.2 (Fig.3.6). Such flow is basically 1 dimensional, in which all turbulence quantities are only functions of $y$. Eq.(2.20) defines the turbulent kinetic energy (TKE) distribution in spectral space, i.e. $E(k, k_t)$. Thus, a spatial-spectral distribution of TKE is defined as follow:

$$E(k, y) = E(k, k_t(y)),$$

which satisfies the following normalization condition:

$$k_t(y) = \int_0^\infty E(k, k_t(y))\,\mathrm{d}k.$$

Such distribution of channel flow (Fig.2.2) gives a special insight of the energy distribution and flow structure of turbulence field. In most part of the flow field which is far away from wall, most of turbulent kinetic energy concentrate in a very narrow area of spectral space, which only consists a small portion of computational cost in the simulation. In the turbulent boundary layer near the wall, the distribution of TKE in spectral space becomes very wide and considerably increases the computational cost. Based on the generation method in Section 2.1, a scale-reduction algorithm is designed to cut off unnecessary computation while still capture the energetic struc-

tures in the flow field. Define the error $e$ representing the energy loss ratio in order to reduce computational cost:

$$e = 1 - \frac{k_t^e}{k_t}.$$

Define two boundary curves $\Gamma_1(y)$, $\Gamma_2(y)$ as follow:

$$\int_{\Gamma_1^e(y)}^{\Gamma_2^e(y)} E(k, y)\, \mathrm{d}k = k_t^e(y).$$

The generation process only need to be operated in a small band of physical-spectral space (Fig.2.2) between $\Gamma_1$ and $\Gamma_2$ to reconstruct most of TKE up to an error $e$.



(a) spatial-spectral distribution of TKE  (b) Cut off boundaries
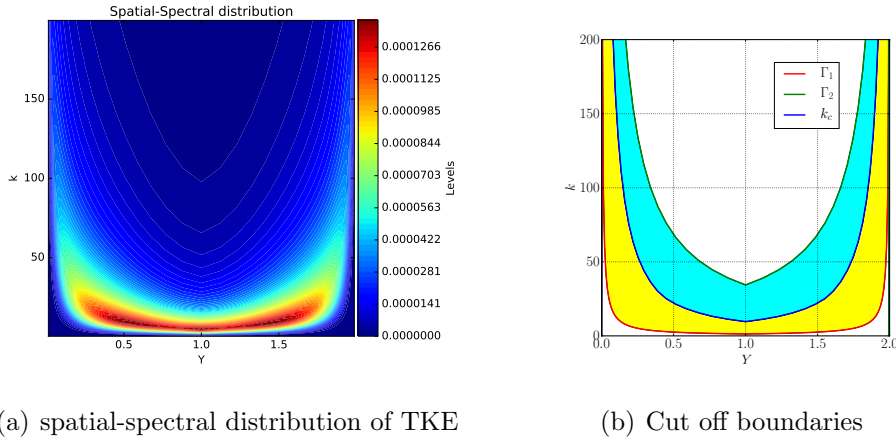
Figure 2.2.    Channel flow: (a) presents TKE distribution in physical-spectral space. (b) shows the regions and cutoff bounds for turbulence generation. Generation process is only conducted in yellow and blue regions using different time-advance procedures proposed in Sec.2.1.2. Yellow part is large scale generation with smaller wavenumber. Blue part is small scale with large wavenumber. White-colored area is discarded in generation process.

# 3. NUMERICAL RESULTS

## 3.1 Isotropic homogeneous turbulence

### 3.1.1 Spatial structure

Generation of isotropic homogeneous turbulence is an important way to validate various properties of turbulence synthesis models. An isotropic homogeneous turbulence case is computed in order to verify the model constructed in Methodology section. Because RANS type model cannot compute $k_t$ and $\epsilon$ of isotropic homogeneous turbulence, such data is obtained from previous DNS results (Kaneda et al. [2003]). Spectrum of generated turbulence with different modes and different resolution are compared with von-Karman spectrum (Fig.3.1). Wavenumbers of modes are generated with the following formula (Juves [1999]):

$$k_n = \exp[\ln k_0 + n d_k], n = 0, 1, 2, .....M,$$

where $k_0$ is the first wavenumber of the sequence, $d_k$ is a parameter to control the distances between wavenumbers. Another quantity that could be used to exam spatial structure of generated turbulence is the structure function defined as follow:

$$D_{11}(r, 0, 0) = \langle [u(x + r, y, z, t) - u(x, y, z, t)]^2 \rangle,$$

$$D_{22}(0, r, 0) = \langle [u(x, y + r, z, t) - u(x, y, z, t)]^2 \rangle,$$

$$D_{33}(0, 0, r) = \langle [u(x, y, z + r, t) - u(x, y, z, t)]^2 \rangle.$$

From previous theoretical and experimental research (Fung et al. [1992],Ishihara et al. [2009],etc.), second order structure function has the following form in inertial sub-range:

$$D_{11} = D_{22} = D_{33} = C' \epsilon^{\frac{2}{3}} r^{\frac{2}{3}},$$
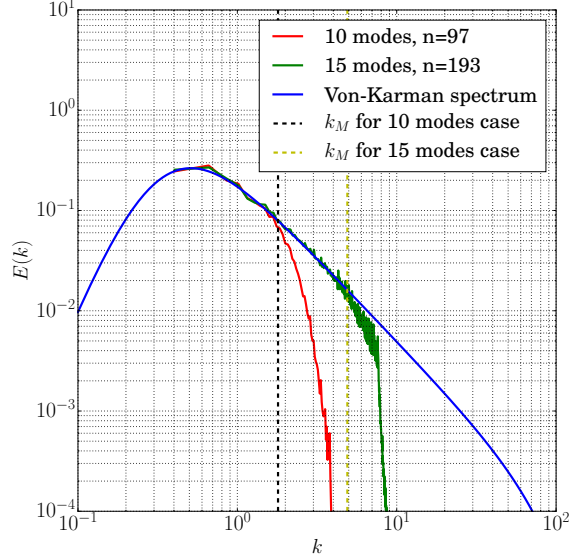
Figure 3.1. Spectrum of generated turbulence: In this simulation $k_t = 0.5$, $\nu = 7 \times 10^{-4}$, $\epsilon = 0.0849$ are nondimensional parameters from previous DNS results. $k_{min}$ is the cutoff wavenumber of original simulation representing the largest scale. $k_0 = 0.3$, $d_k = 0.2$ for wavenumber generation. The result shows good agreement with input spectrum within the range of wavenumbers of modes used in the generation. With mode number increased, the spectrum range that could be accurately captured gets larger. $k_M$ is the largest wavenumber used in generation. Normally $k_M \leqslant k_N$. $k_N$ is the Nyquist wavenumber of mesh.

where $C'$ is a constant. In Fung et al. [1992] the value of $C'$ is equal to 1.7. Numerical results of $D_{11}$, $D_{22}$ and $D_{33}$ are compared with theoretical solutions (Fig.3.2). The energy spectrum results and second order structural function results indicates that this turbulence generation method gives right spatial turbulence structure in homogeneous isotropic cases. The iso-surface of the numerical results are shown in Fig.3.3.



(a) 10 modes, n=97　　　　　　　　(b) 15 modes, n=193
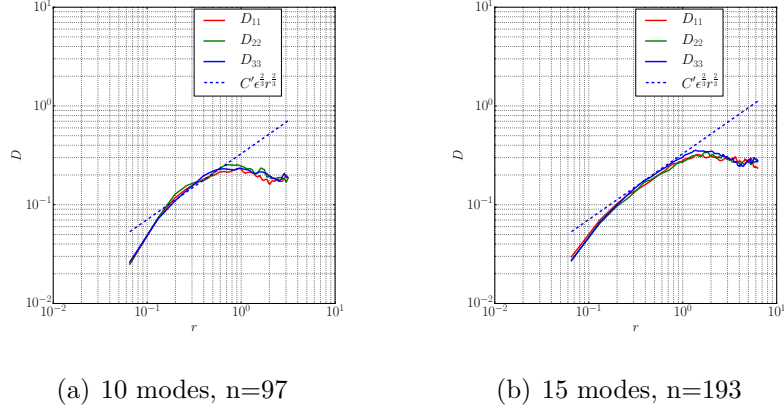
Figure 3.2. Second order structure functions of simulations with different number of modes and grid points. Dashed lines are theoretical results with constant $C' = 1.7$. The simulation shows good agreement compared with theoretical results in inertial subrange.

### 3.1.2   Time correlation

The Eulerian autocorrelation is defined as follow:

$$R_{uu}^E(\tau) = \langle u(t)u(t+\tau)\rangle,$$

$$R_{vv}^E(\tau) = \langle v(t)v(t+\tau)\rangle,$$

$$R_{ww}^E(\tau) = \langle w(t)w(t+\tau)\rangle.$$

The normalized Eulerian autocorrelation can be computed as follow:

$$R_{11}^{E,N}(\tau) = \frac{R_{uu}^E(\tau)}{R_{uu}^E(0)},$$

(a) Isosurface of $u$          (b) Isosurface of $v$

(c) Isosurface of $w$          (d) Isosurface of $w$
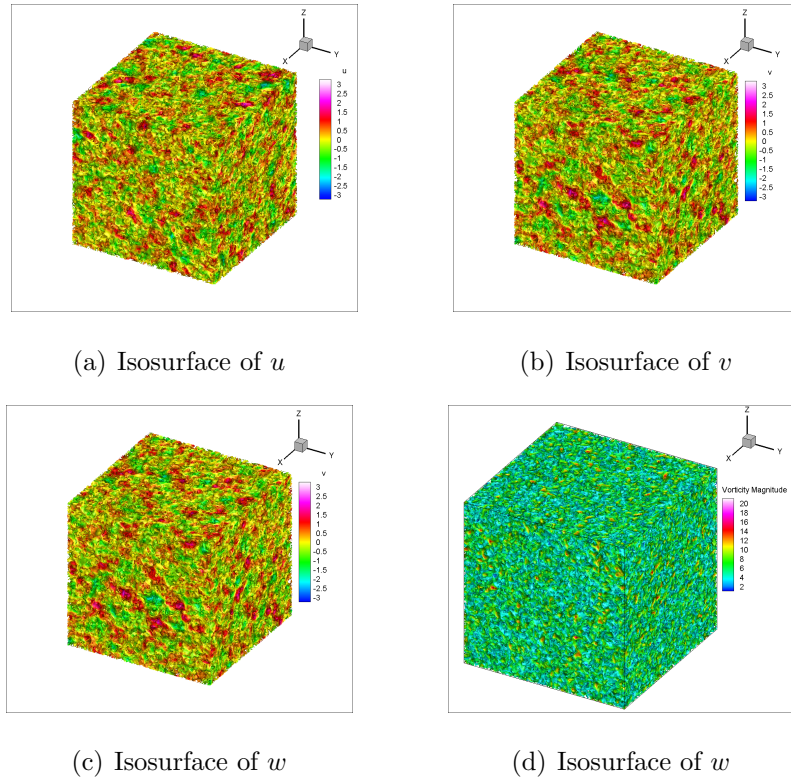
Figure 3.3. Isosurface of vorticity magnitude

Figure 3.4. Iso-surface of velocity components and vorticity magnitude. Flow structures of different scales can be observed in the flow field. Also, the generated flow field is homogeneous and isotropic.

$$R_{22}^{E,N}(\tau) = \frac{R_{vv}^E(\tau)}{R_{vv}^E(0)},$$

$$R_{33}^{E,N}(\tau) = \frac{R_{ww}^E(\tau)}{R_{ww}^E(0)}.$$

The Eulerian frequency spectrums are defined as the Fourier transform of Eulerian autocorrelation:

$$\Phi_{uu}^E(\omega) = \int_{\mathbb{R}} R_{uu}^E(\tau)\, e^{-i\omega\tau}\, d\tau,$$

$$\Phi_{vv}^E(\omega) = \int_{\mathbb{R}} R_{vv}^E(\tau)\, e^{-i\omega\tau}\, d\tau,$$

$$\Phi_{ww}^E(\omega) = \int_{\mathbb{R}} R_{ww}^E(\tau)\,\mathrm{e}^{-i\omega\tau}\,\mathrm{d}\tau.$$

Fung et al. [1992],Ishihara et al. [2009] suggest that for isotropic homogeneous turbulence, Eulerian frequency spectrum in inertial subrange can be approximated as follows:

$$\Phi_{uu}^E(\omega) = \Phi_{vv}^E(\omega) = \Phi_{ww}^E(\omega) \approx C^E \epsilon^{\frac{2}{3}} \langle u_1^2 \rangle \omega^{-\frac{5}{3}},$$

where $C^E = 0.46$ is a constant from Ishihara et al. [2009]. Results of Eulerian autocorrelation and frequency spectrum are shown in Fig.3.5.
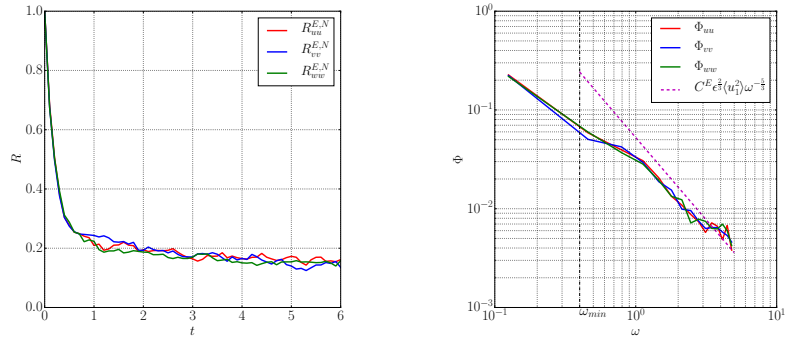


(a) Normalized Eulerian auto-correlation

(b) Eulerian frequency spectrum

Figure 3.5. Eulerian temporal and frequency properties of simulation results. Frequency spectrums are compared with analytical results from previous study. $\omega_{min}$ is the lower boundary of frequency inertial subrange. It can be observed that the Eulerian frequency spectrums of the numerical results approximate the theoretical solution in the inertial subrange, especially at high frequency.

## 3.2 Fully Developed Turbulent Channel Flow

RANS data of channel flow case in Fig. 3.6 was computed using Reynolds Stress Model to obtain full Reynolds stress and turbulence dissipation rate. Turbulent boundary layer was fully resolved, including several grid points in viscous sublayer.

This RANS data is used as input data for turbulence generation. Residual of RSM simulation results are in Table 3.1.

Table 3.1.

Residuals

| Equation | Continuity | $x$ momentum | $y$ momentum | $z$ momentum | $k$ equation |
|---|---|---|---|---|---|
| Residual | $1.23 \times 10^{-6}$ | $2.04 \times 10^{-6}$ | $7.04 \times 10^{-9}$ | $6.61 \times 10^{-9}$ | $2.3044 \times 10^{-6}$ |

| Equation | $\epsilon$ | $\langle uu \rangle$ | $\langle vv \rangle$ | $\langle ww \rangle$ | $\langle uv \rangle$ |
|---|---|---|---|---|---|
| Residual | $5.81 \times 10^{-6}$ | $5.59 \times 10^{-6}$ | $5.72 \times 10^{-6}$ | $5.68 \times 10^{-6}$ | $5.44 \times 10^{-6}$ |
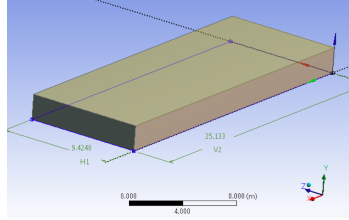


(a) Geometry setup
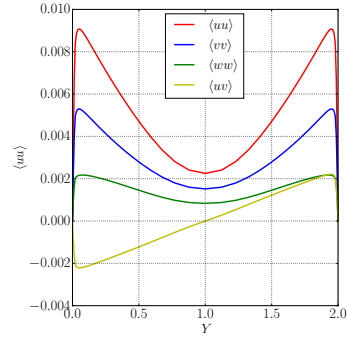
(b) RANS data

Figure 3.6. Channel flow: (a) is geometry setup of this channel flow, X is the streamwise direction of the channel flow. $Z = 0$ and $Z = 3\pi$ are periodic boundaries. $Y = 0$ and $Y = 2$ are no-slip boundaries. Gradient of mean turbulence field only exist on $Y$ direction, while $X$ and $Z$ direction are uniform. (b) is RANS data of this channel flow from standard Reynolds stress model simulation.

Fig. 3.7 shows TKE reconstruction at different wavenumbers. It can be observed that most of turbulent kinetic energy was fully reconstructed except for very high wavenumber case ($k = 81.34$). Also for each wavenumber, the energy of generated turbulence fluctuation concentrates at the neighbor of wavenumber of specific

wavelet basis, which is the result of Eq. 2.7, 2.9. The reconstruction process is done in separated regions because of different time-advance schemes in Section 2.1.2. For $k = 40.00$ and $k = 81.34$, there is a region in which the reconstructed energy is 0. It is because that TKE at this wavenumber only contributes to very small portion of total TKE at this region, thus is cutoff by the algorithm in Section 2.4. This portion of TKE can be accurately reconstructed, but the computation cost will increase significantly and the result does not change much. At very high wavenumber (Fig.3.7(g), 3.7(h)), although characteristic wavenumber of the wavelet mode is still below Nyquist wavenumber (in this case, $k_N$=120), some part of energy of the wavelet mode goes beyond $k_N$, which cannot be captured by the mesh in this case.

Fig. 3.8 shows the comparison of Reynolds stress from RANS data and reconstructed Reynolds stress. It can be observed that reconstructed $\langle uu \rangle$, $\langle vv \rangle$, $\langle ww \rangle$, $\langle uv \rangle$ agree with RANS data. It should be noticed that RANS data used in Fig. 3.8 is slightly different from the data in Fig. 3.6. Define reconstruction ratio as the follow:

$$\gamma = \frac{\int_0^{k_N} E(k, y) \, \mathrm{d}k}{k_t(y)}.$$

$\gamma$ represents the part of turbulent kinetic energy that could be resolved for given mesh. Then resolvable Reynolds stress $\langle \boldsymbol{uu} \rangle^\gamma$ is defined as follow:

$$\langle \boldsymbol{uu} \rangle^\gamma = \gamma \langle \boldsymbol{uu} \rangle.$$

$\langle \boldsymbol{uu} \rangle^\gamma$ represents the best approximation of Reynolds stress given a mesh of Nyquist wavenumber $k_N$. The reconstructed Reynolds stress in Fig. 3.8 shows good agreement with $\langle \boldsymbol{uu} \rangle^\gamma$ from RANS data.

Iso-contour of 3 total velocity components $U$, $V$, $W$ are shown in Fig. 3.9. The reconstructed velocity field shows very realistic flow image. Large scale spatial structures are distributed near the centering line of channel. Near the wall turbulence structures get smaller and damping effect of the boundary starts to dominate. $V$ and $W$ components are close to 0, with some random fluctuation distributed in the cross section.

(a) $k = 3.0$

(b) $k = 3.0$

(c) $k = 7.38$

(d) $k = 7.38$

(e) $k = 40.00$

(f) $k = 40.00$

(g) $k = 81.34$

(h) $k = 81.34$
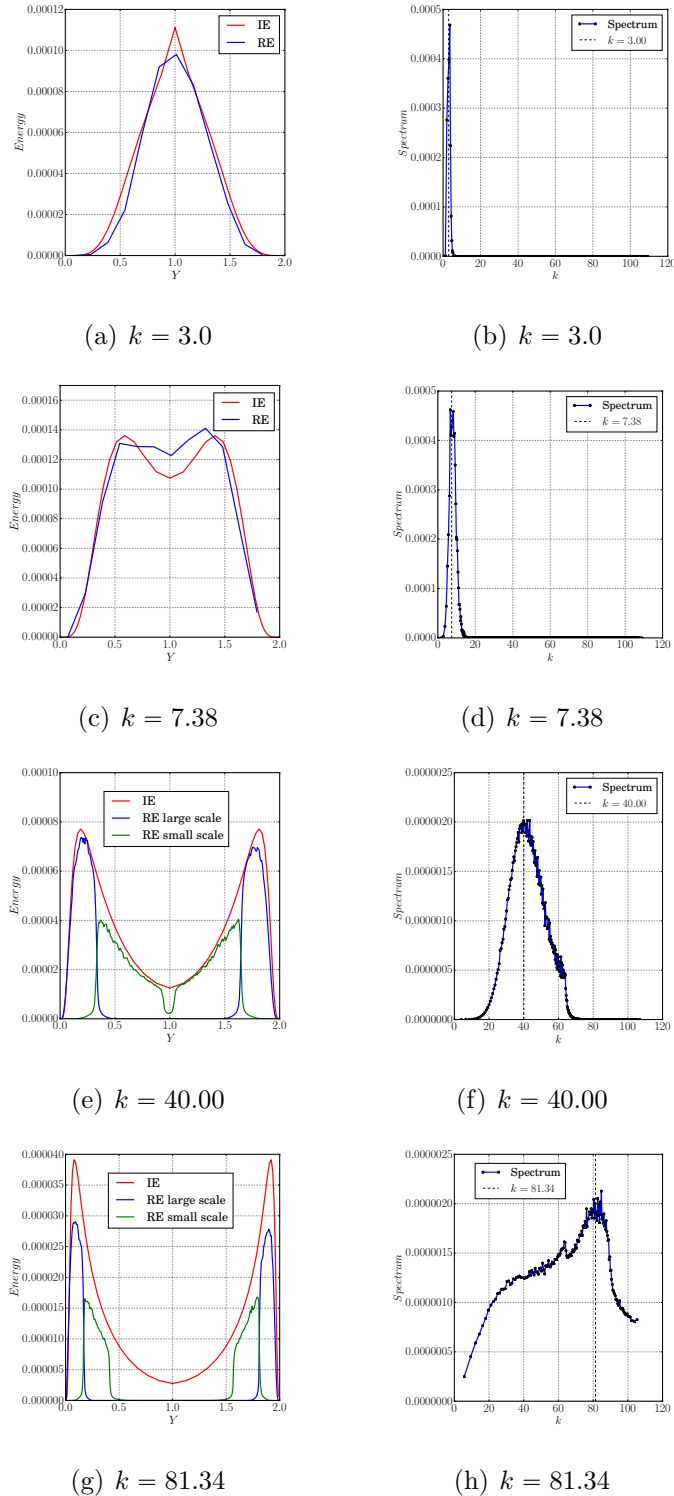
Figure 3.7. Reconstruction of TKE at different wavenumber. Left column: spatial distribution of TKE at certain wavenumber. Red line: Input energy at certain $k$. Blue line: reconstructed energy of large scale at $k$. Green line: reconstructed energy of small scale at $k$. Right column: spectral distribution of TKE. IE: Input Energy. RE: Reconstructed Energy.

(a) $\langle uu \rangle$

(b) $\langle vv \rangle$

(c) $\langle ww \rangle$

(d) $\langle uv \rangle$
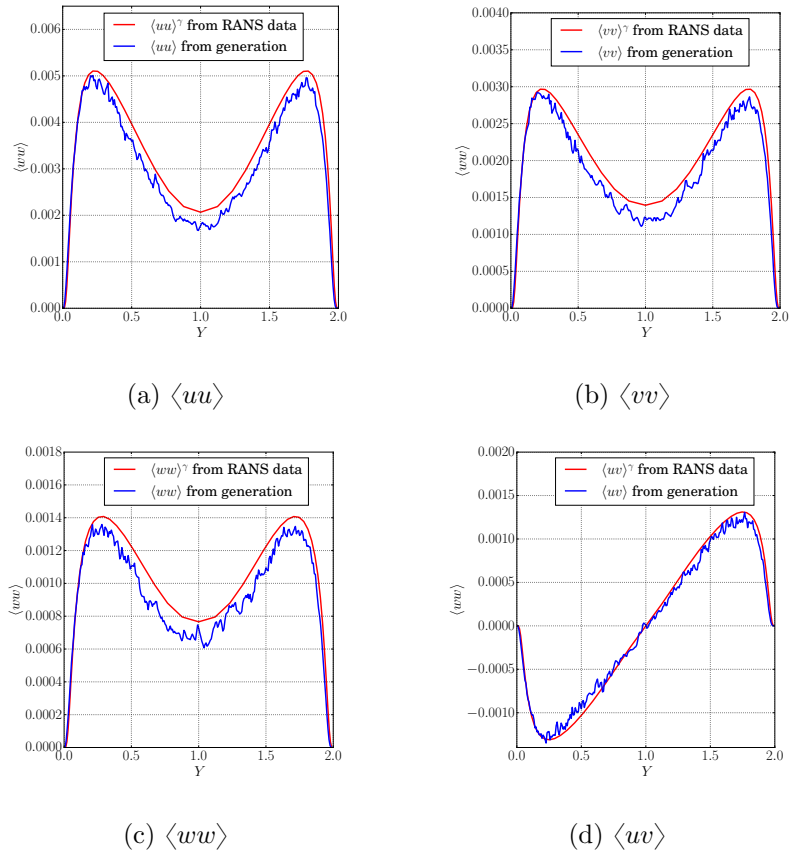
Figure 3.8. Reconstruction of Reynolds stress distributions: The reconstructed Reynolds stress is compared with resolvable Reynolds stress from RANS data. Four main reconstructed Reynolds stresses all show good agreement with resolvable Reynolds stress.

(a) Iso-contour of $U$

(b) Iso-contour of $V$
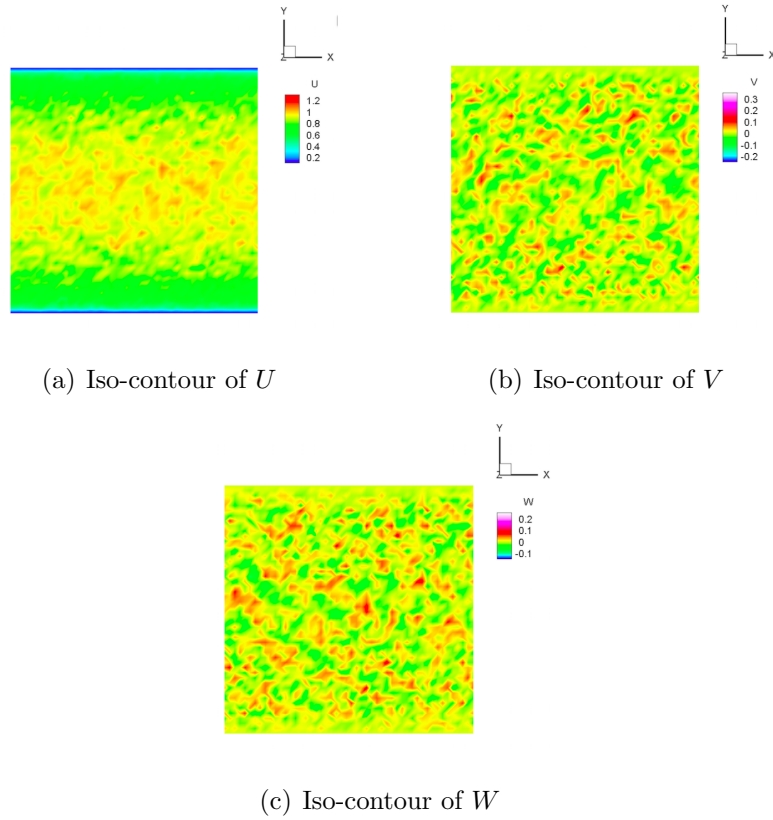
(c) Iso-contour of $W$

Figure 3.9. Iso-contour of different total velocity components $(U, V, W)$ of generated fully developed turbulent channel flow.

# Part III

# Turbulence Deconvolution using Optimization on Quotient Manifold

## 4. PROBLEM SETUP

Filtering of a velocity field $\boldsymbol{u}$ is described by convolution:

$$\tilde{\boldsymbol{u}}(\boldsymbol{x}) = G * \boldsymbol{u} = \iiint G(\boldsymbol{x} - \boldsymbol{y})\boldsymbol{u}(\boldsymbol{y})\,\mathrm{d}^3\boldsymbol{y}. \tag{4.1}$$

If $G$ is known a priori, then $\boldsymbol{u}$ could be found simply using convolution theorem:

$$\widehat{\tilde{\boldsymbol{u}}} = \widehat{G}\widehat{\boldsymbol{u}}, \tag{4.2}$$

$$\boldsymbol{u} = \widetilde{\left(\frac{\widehat{\tilde{\boldsymbol{u}}}}{\widehat{G}}\right)}, \tag{4.3}$$

as long as $\widehat{G} \neq 0$. However, this approach does not work in problems without information about the form of $G$. In a discretized form, Eq. (4.1) can be rewritten as:

$$\tilde{\mathbf{u}} = \mathbf{g} \star \mathbf{u}, \tag{4.4}$$

where $\mathbf{u}$ is a flattened vector of discretized velocity data of size $L$. $\mathbf{g}$ is discretized form of $G$ which is flattened by the same order. $\mathbf{u}, \mathbf{g} \in \mathbb{C}^L$. $\star$ is the circular convolution operator of two vectors of the same length. To make this problem well-posed, it is necessary to assume that $\mathbf{u}$ and $\mathbf{g}$ live in certain subspaces of $\mathbb{C}^L$ (Huang and Hand [2017]), i.e.:

$$\mathbf{g} = \mathbf{B}h, \qquad h \in \mathbb{C}^K, \tag{4.5}$$

$$\mathbf{u} = \overline{\mathbf{C}m}, \qquad m \in \mathbb{C}^N. \tag{4.6}$$

Normally in order to make this problem well-posed, the following relation of dimensions need to be ensured:

$$K + N < L < KN. \tag{4.7}$$

Take DFT of Eq. (4.4):

$$\mathbf{F}\tilde{\mathbf{u}} = (\mathbf{Fg}) \odot (\mathbf{Fu}). \tag{4.8}$$

Plug Eq. (4.5), (4.6) into Eq. (4.8):

$$\mathbf{F}\tilde{\mathbf{u}} = (\mathbf{F}\mathbf{B}h) \odot (\mathbf{F}\overline{\mathbf{C}m}). \tag{4.9}$$

3-D wavelet space is chosen as the subspace in which $\mathbf{u}$ lives, i.e. $\mathbf{C} = \mathbf{W}$, where $\mathbf{W} \in \mathbb{C}^{L \times N}$ is 3-D inverse wavelet transform matrix. $\mathbf{B}$ represents the support set of filter $\mathbf{g}$. 4.8 can be further turned into an optimization problem with the following cost function:

$$f : \mathcal{N} \to \mathbb{R}, \mathcal{N} = \mathbb{C}_*^K \times \mathbb{C}_*^N,$$
$$(h, m) \mapsto \| \mathbf{F}\tilde{\mathbf{u}} - diag(\mathbf{F}\mathbf{B}hm^*\mathbf{W}^*\mathbf{F}^{-1}) \|_2^2 . \tag{4.10}$$

However, such minimizer is not unique since given a solution $(h_\#, m_\#)$, $(h_\# p^{-1}, m_\# p)$ will also be a solution, where $p \in \mathbb{C}$. Denote $[(h, m)] = \{(hp^{-1}, mp) | p \in \mathbb{C}_*\}$ as the equivalent class under group action $GL(1)$. Define quotient manifold $\mathcal{Q} = \mathbb{C}_*^K \times \mathbb{C}_*^N / \mathbb{C}_* = \{[(h, m)] | (h, m) \in \mathbb{C}_*^K \times \mathbb{C}_*^N\}$. Then the cost function Eq. (4.10) can be restated on $\mathcal{Q}$:

$$f : \mathcal{Q} \to \mathbb{R},$$
$$(h, m) \mapsto \| \mathbf{F}\tilde{\mathbf{u}} - diag(\mathbf{F}\mathbf{B}hm^*\mathbf{W}^*\mathbf{F}^{-1}) \|_2^2 . \tag{4.11}$$

Hence the deconvolution problem Eq. (4.1) can be transformed into an optimization problem on a quotient manifold.

## 5. WAVELETS AND DIVERGENCE-FREE WAVELETS

### 5.1 Multiresolution Analysis and 1-D Wavelet

A Multiresolution Analysis of $L^2(\mathbb{R})$ is a sequence of subspaces $(V_j)_{j\in\mathbb{Z}}$ verifying (Hernández and Weiss [1996]):

(1) $\forall j, V_j \subset V_{j+1}, \cap_{j\in\mathbb{Z}} V_j = 0, \cup_{j\in\mathbb{Z}} V_j$ is dense in $L^2(\mathbb{R})$.

(2) $f \in V_j \iff f(2\cdot) \in V_{j+1}$.

(3)There exists a function $\phi \in V_0$ such that the family $\{\phi(\cdot - k); k \in \mathbb{Z}\}$ forms a Riesz basis of $V_0$.

$V_j$ is spanned by $\{\phi_{j,k}; k \in \mathbb{Z}\}$, in which $\phi_{j,k}(x) = 2^{j/2}\phi(2^j x - k)$ is called the scaling function. Wavelet space $W_j$ appears as complementary space of $V_j$:

$$V_{j+1} = V_j \bigoplus W_j. \tag{5.1}$$

There exists a function $\psi(\cdot)$ such that $W_j$ is spanned by $\psi_{j,k}; j, k \in \mathbb{Z}$, where $\psi_{j,k} = 2^{j/2}\psi(2^j \cdot -k)$ are called wavelet functions. For orthogonal wavelets, $f \in L^2(\mathbb{R})$ can be represented as follow:

$$f = \sum_{j\in\mathbb{Z}} \sum_{k\in\mathbb{Z}} d_{j,k}\psi_{j,k}, \tag{5.2}$$

where $d_{j,k} = \langle f, \psi_{j,k} \rangle$ are wavelet coefficients.

### 5.2 MRA of 3-D Scalar and Vector Function Space

MRA of multi-dimensional scalar function is simply tensor product of 1D MRA (Deriaz and Perrier [2006]):

$$\mathcal{V}_\mathbf{j} = V_{j_1}^1 \bigotimes V_{j_2}^2 \bigotimes V_{j_3}^3. \tag{5.3}$$

Orthogonal projection of $f \in L^2(\mathbb{R}^3)$ is as follow:

$$f = \sum_{\mathbf{j}\in\mathbb{Z}} \sum_{\mathbf{k}\in\mathbb{Z}} d_{\mathbf{j},\mathbf{k}}\psi_{\mathbf{j},\mathbf{k}}, \tag{5.4}$$

where $\mathbf{j} = (j_1, j_2, j_3)$, $\mathbf{k} = (k_1, k_2, k_3)$ are multiindexes. $\psi_{\mathbf{j,k}}$ is the tensor-product wavelet basis function defined as follow:

$$\psi_{\mathbf{j,k}}(x_1, x_2, x_3) = \psi^1_{j_1,k_1}(x_1)\psi^2_{j_2,k_2}(x_2)\psi^3_{j_3,k_3}(x_3). \tag{5.5}$$

For three-dimensional vector function $\boldsymbol{u} \in (L^2(\mathbb{R}^3))^3$, MRA can be constructed as a Cartesian product of three-dimensional scalar MRAs:

$$\mathcal{V}_{\mathbf{j_1 j_2 j_3}} = (V^{11}_{j_{11}} \otimes V^{12}_{j_{12}} \otimes V^{13}_{j_{13}}) \times (V^{21}_{j_{21}} \otimes V^{22}_{j_{22}} \otimes V^{33}_{j_{33}}) \times (V^{31}_{j_{31}} \otimes V^{32}_{j_{32}} \otimes V^{33}_{j_{33}}). \tag{5.6}$$

The corresponding orthogonal decomposition is as follow:

$$\Psi_{1,\mathbf{j,k}} = \begin{pmatrix} \psi^{11}(x_1)\psi^{12}(x_2)\psi^{13}(x_3) \\ 0 \\ 0 \end{pmatrix},$$

$$\Psi_{2,\mathbf{j,k}} = \begin{pmatrix} 0 \\ \psi^{21}(x_1)\psi^{22}(x_2)\psi^{23}(x_3) \\ 0 \end{pmatrix}, \tag{5.7}$$

$$\Psi_{3,\mathbf{j,k}} = \begin{pmatrix} 0 \\ 0 \\ \psi^{31}(x_1)\psi^{32}(x_2)\psi^{33}(x_3) \end{pmatrix},$$

$$\boldsymbol{u} = \sum_{i=1}^{3}\sum_{\mathbf{j}\in\mathbb{Z}}\sum_{\mathbf{k}\in\mathbb{Z}} d_{i,\mathbf{j,k}}\Psi_{i,\mathbf{j,k}}. \tag{5.8}$$

## 5.3   Divergence-Free Wavelets

For an MRA $(V^1_j)$ with scaling function $\phi^1_{j,k}$ and wavelet function $\psi^1_{j,k}$, there exists an MRA $(V^0_j)$ with scaling function $\phi^0_{j,k}$ and wavelet function $\psi^0_{j,k}$ such that:

$$\frac{\mathrm{d}\psi^1(x)}{\mathrm{d}x} = 4\psi^0, \qquad \frac{\mathrm{d}\phi^1(x)}{\mathrm{d}x} = \phi^0(x) - \phi^0(x-1). \tag{5.9}$$

This pair of MRA $(V^1_j)$ and $(V^0_j)$ related with integration and differentiation can be used to construct divergence-free wavelets. Divergence-Free wavelet has been

constructed and extended to arbitrary dimension (Deriaz and Perrier [2009], Urban [2012]). Here anisotropic multidimemsion wavelets are used for decomposition and further analysis of turbulent flow. Consider an MRA of 3-D vector function space as follow:

$$\mathcal{V}_{\mathbf{j}_1\mathbf{j}_2\mathbf{j}_3} = (V^1_{1,j_1} \otimes V^0_{1,j_2} \otimes V^0_{1,j_3}) \times (V^0_{2,j_1} \otimes V^1_{2,j_2} \otimes V^0_{2,j_3}) \times (V^0_{3,j_1} \otimes V^0_{3,j_2} \otimes V^1_{3,j_3}).$$
(5.10)

Three sets of wavelet basis appear in this MRA:

$$\Psi_{1,\mathbf{j},\mathbf{k}} = \begin{pmatrix} \psi^1(x_1)\psi^0(x_2)\psi^0(x_3) \\ 0 \\ 0 \end{pmatrix},$$

$$\Psi_{2,\mathbf{j},\mathbf{k}} = \begin{pmatrix} 0 \\ \psi^0(x_1)\psi^1(x_2)\psi^0(x_3) \\ 0 \end{pmatrix},$$
(5.11)

$$\Psi_{3,\mathbf{j},\mathbf{k}} = \begin{pmatrix} 0 \\ 0 \\ \psi^0(x_1)\psi^0(x_2)\psi^1(x_3) \end{pmatrix},$$

$$\boldsymbol{u} = \sum_{i=1}^{3}\sum_{\mathbf{j}\in\mathbb{Z}}\sum_{\mathbf{k}\in\mathbb{Z}} d_{i,\mathbf{j},\mathbf{k}}\Psi_{i,\mathbf{j},\mathbf{k}}.$$
(5.12)

Divergence-free wavelet takes the following form (Deriaz and Perrier [2009]):

$$\Psi^{div}_{1,\mathbf{j},\mathbf{k}} = \begin{pmatrix} 2^{j_2}\psi^1(x_1)\psi^0(x_2)\psi^0(x_3) \\ -2^{j_1}\psi^0(x_1)\psi^1(x_2)\psi^0(x_3) \\ 0 \end{pmatrix},$$

$$\Psi^{div}_{2,\mathbf{j},\mathbf{k}} = \begin{pmatrix} 0 \\ 2^{j_3}\psi^0(x_1)\psi^1(x_2)\psi^0(x_3) \\ -2^{j_2}\psi^0(x_1)\psi^0(x_2)\psi^1(x_3) \end{pmatrix},$$
(5.13)

$$\Psi^{div}_{3,\mathbf{j},\mathbf{k}} = \begin{pmatrix} -2^{j_3}\psi^1(x_1)\psi^0(x_2)\psi^0(x_3) \\ 0 \\ 2^{j_1}\psi^0(x_1)\psi^0(x_2)\psi^1(x_3) \end{pmatrix},$$

$$\boldsymbol{u} = \sum_{i=1}^{3} \sum_{\mathbf{j} \in \mathbb{Z}^3} \sum_{\mathbf{k} \in \mathbb{Z}^3} d_{i,\mathbf{j},\mathbf{k}}^{div} \Psi_{i,\mathbf{j},\mathbf{k}}^{div} + \sum_{\mathbf{j} \in \mathbb{Z}^3} \sum_{\mathbf{k} \in \mathbb{Z}^3} d_{\mathbf{j},\mathbf{k}}^{n} \Psi_{\mathbf{j},\mathbf{k}}^{n}. \tag{5.14}$$

According to Deriaz and Perrier [2009], 3-D divergence-free and non-divergence-free wavelet coefficients are related by the following linear system:

$$\begin{bmatrix} 2^{j_2} & 0 & -2^{j_3} & 2^{j_1} \\ -2^{j_1} & 2^{j_3} & 0 & 2^{j_2} \\ 0 & -2^{j_2} & 2^{j_1} & 2^{j_3} \\ 2^{j_3} & 2^{j_1} & 2^{j_2} & 0 \end{bmatrix} \begin{bmatrix} d_{1,\mathbf{j},\mathbf{k}}^{div} \\ d_{2,\mathbf{j},\mathbf{k}}^{div} \\ d_{3,\mathbf{j},\mathbf{k}}^{div} \\ d_{i,\mathbf{j},\mathbf{k}}^{n} \end{bmatrix} = \begin{bmatrix} d_{i,\mathbf{j},\mathbf{k}} \\ d_{i,\mathbf{j},\mathbf{k}} \\ d_{i,\mathbf{j},\mathbf{k}} \\ 0 \end{bmatrix}. \tag{5.15}$$

Eq. (5.15) offers a method to find divergence-free wavelet coefficients using non-divergence-free wavelet coefficients (anisotropic wavelets), which could be obtained using the Fast Wavelet Transform without any numerical integration.

## 6. FAST WAVELET TRANSFORM

### 6.1 Dual Basis and Scaling Equations

For any given 1-D MRA $(V_j)_{j \in \mathbb{Z}}$ with scaling mother function $\phi(\cdot)$ and wavelet mother function $\psi(\cdot)$, a unique pair of dual scaling mother function $\phi^*(\cdot)$ and wavelet mother function $\psi^*(\cdot)$ can be found which satisfies the following biorthogonal properties (Deriaz and Perrier [2006]):

$$\langle \phi | \phi_k^* \rangle = \delta_{k,0}, \langle \phi | \psi_{j,k}^* \rangle = 0, \langle \psi | \psi_{j,k}^* \rangle = \delta_{j,0}\delta_{k,0}, \langle \psi | \phi_k^* \rangle = 0, \tag{6.1}$$

in which $\phi_k^*$ and $\psi_{j,k}^*$ have the same structure as $\phi_k$ and $\psi_{j,k}$:

$$\phi_k^* = \phi^*(\cdot - k)\psi_{j,k}^* = 2^{j/2}\psi^*(2^j \cdot - k). \tag{6.2}$$

From the definition of MRA in Sec. 5.1, there exists sequence $h_k$ and $g_k$ satisfying:

$$\frac{1}{\sqrt{2}}\phi\left(\frac{x}{2}\right) = \sum_{k \in \mathbb{Z}} h_k \phi(x - k), \tag{6.3}$$

$$\frac{1}{\sqrt{2}}\psi\left(\frac{x}{2}\right) = \sum_{k \in \mathbb{Z}} g_k \phi(x - k). \tag{6.4}$$

Similarly for the dual basis:

$$\frac{1}{\sqrt{2}}\phi^*\left(\frac{x}{2}\right) = \sum_{k \in \mathbb{Z}} h_k^* \phi^*(x - k), \tag{6.5}$$

$$\frac{1}{\sqrt{2}}\psi^*\left(\frac{x}{2}\right) = \sum_{k \in \mathbb{Z}} g_k^* \phi^*(x - k). \tag{6.6}$$

### 6.2 1-D Decomposition and Reconstruction Algorithms

For $f \in L^2(\mathbb{R})$, the projection of $f$ on $V_j$ with index $j \in \mathbb{Z}$ is as follow:

$$f_J(x) = 2^{\frac{J}{2}} \sum_{k \in \mathbb{Z}} c_{J,k} \phi(2^J x - k). \tag{6.7}$$

For two neighboring layers of MRA representation, the scale relation Eq. (6.3) to Eq. (6.6) can be used to form a relation of $c_{j,k}$ and $d_{j,k}$ between neighboring layers(Kahane et al. [1995],Daubechies [1992]):

$$
\begin{aligned}
c_{j,k} &= \sum_l h_l^* c_{j+1,l+2k}, \\
d_{j,k} &= \sum_l g_l^* c_{j+1,l+2k}.
\end{aligned}
\tag{6.8}
$$

Typically such iteration need a initial set of coefficients $c_{J,k}$ to start, where $J$ is the largest value for the wavelet representation. For discretized data on a uniform stencil, the data on the stencil is used directly as $c_{J,k}$ to compute DWT coefficients (Mallat [1999]). Reconstruction two-layer relation is as follow:

$$
c_{j+1,k} = \sum_l (h_{k-2l} c_{j,l} + g_{k-2l} d_{j,l}).
\tag{6.9}
$$

Such decomposition and reconstruction formulas ensure that after a decomposition and reconstruction process, the data could be recovered exactly, up to machine precision.

For real data with a finite length, this transform algorithm is not applicable without special treatment on the boundary. Also, there will be difficulty if the length of this series is not $2^n$. The treatment used here is to complement the series to length of $2^n$ with some integer $n$, and periodically extend this series, such that this transform algorithm could be used (Mallat [1999]).

## 6.3    Decomposition and Reconstruction formulas of 3-D vector functions

For 3-D MRA of the form Eq. (5.3), the decomposition formula is as follow:

$$c_{j_1-1,j_2,j_3,k_1,k_2,k_3} = \sum_l h_l^{*1} c_{j_1,j_2,j_3,l+2k_1,k_2,k_3},$$

$$c_{j_1,j_2-1,j_3,k_1,k_2,k_3} = \sum_l h_l^{*2} c_{j_1,j_2,j_3,k_1,l+2k_2,k_3},$$

$$c_{j_1,j_2,j_3-1,k_1,k_2,k_3} = \sum_l h_l^{*3} c_{j_1,j_2,j_3,k_1,k_2,l+2k_3},$$

$$d_{j_1-1,j_2,j_3,k_1,k_2,k_3} = \sum_l g_l^{*1} c_{j_1,j_2,j_3,l+2k_1,k_2,k_3},$$

$$d_{j_1,j_2-1,j_3,k_1,k_2,k_3} = \sum_l g_l^{*2} c_{j_1,j_2,j_3,k_1,l+2k_2,k_3},$$

$$d_{j_1,j_2,j_3-1,k_1,k_2,k_3} = \sum_l g_l^{*3} c_{j_1,j_2,j_3,k_1,k_2,l+2k_3}.$$

$$(6.10)$$

Reconstruction iteration can be similarly reconstructed as 1-D case:

$$c_{j_1+1,j_2,j_3,k_1,k_2,k_3} = \sum_l (h_{k-2l}^1 c_{j_1,j_2,j_3,l,k_2,k_3} + g_{k-2l}^1 d_{j_1,j_2,j_3,l,k_2,k_3}),$$

$$c_{j_1,j_2+1,j_3,k_1,k_2,k_3} = \sum_l (h_{k-2l}^2 c_{j_1,j_2,j_3,k_1,l,k_3} + g_{k-2l}^2 d_{j_1,j_2,j_3,k_1,l,k_3}),$$

$$c_{j_1,j_2,j_3+1,k_1,k_2,k_3} = \sum_l (h_{k-2l}^3 c_{j_1,j_2,j_3,k_1,k_2,l} + g_{k-2l}^3 d_{j_1,j_2,j_3,k_1,k_2,l}).$$

$$(6.11)$$

Fast Wavelet Transform of 3-D vector function with the MRA Eq. (5.10) can be achieved by applying Eq. (6.10) and Eq. (6.11) to each velocity components:

$$c^u_{j_1-1,j_2,j_3,k_1,k_2,k_3} = \sum_l h^{*1}_l c^u_{j_1,j_2,j_3,l+2k_1,k_2,k_3},$$

$$c^u_{j_1,j_2-1,j_3,k_1,k_2,k_3} = \sum_l h^{*0}_l c^u_{j_1,j_2,j_3,k_1,l+2k_2,k_3},$$

$$c^u_{j_1,j_2,j_3-1,k_1,k_2,k_3} = \sum_l h^{*0}_l c^u_{j_1,j_2,j_3,k_1,k_2,l+2k_3},$$

$$d^u_{j_1-1,j_2,j_3,k_1,k_2,k_3} = \sum_l g^{*1}_l c^u_{j_1,j_2,j_3,l+2k_1,k_2,k_3},$$

$$d^u_{j_1,j_2-1,j_3,k_1,k_2,k_3} = \sum_l g^{*0}_l c^u_{j_1,j_2,j_3,k_1,l+2k_2,k_3}, \qquad (6.12)$$

$$d^u_{j_1,j_2,j_3-1,k_1,k_2,k_3} = \sum_l g^{*0}_l c^u_{j_1,j_2,j_3,k_1,k_2,l+2k_3},$$

$$c^u_{j_1+1,j_2,j_3,k_1,k_2,k_3} = \sum_l (h^1_{k-2l} c^u_{j_1,j_2,j_3,l,k_2,k_3} + g^1_{k-2l} d^u_{j_1,j_2,j_3,l,k_2,k_3}),$$

$$c^u_{j_1,j_2+1,j_3,k_1,k_2,k_3} = \sum_l (h^0_{k-2l} c^u_{j_1,j_2,j_3,k_1,l,k_3} + g^0_{k-2l} d^u_{j_1,j_2,j_3,k_1,l,k_3}),$$

$$c^u_{j_1,j_2,j_3+1,k_1,k_2,k_3} = \sum_l (h^0_{k-2l} c^u_{j_1,j_2,j_3,k_1,k_2,l} + g^0_{k-2l} d^u_{j_1,j_2,j_3,k_1,k_2,l}).$$

$$c^v_{j_1-1,j_2,j_3,k_1,k_2,k_3} = \sum_l h^{*0}_l c^v_{j_1,j_2,j_3,l+2k_1,k_2,k_3},$$

$$c^v_{j_1,j_2-1,j_3,k_1,k_2,k_3} = \sum_l h^{*1}_l c^v_{j_1,j_2,j_3,k_1,l+2k_2,k_3},$$

$$c^v_{j_1,j_2,j_3-1,k_1,k_2,k_3} = \sum_l h^{*0}_l c^v_{j_1,j_2,j_3,k_1,k_2,l+2k_3},$$

$$d^v_{j_1-1,j_2,j_3,k_1,k_2,k_3} = \sum_l g^{*0}_l c^v_{j_1,j_2,j_3,l+2k_1,k_2,k_3},$$

$$d^v_{j_1,j_2-1,j_3,k_1,k_2,k_3} = \sum_l g^{*1}_l c^v_{j_1,j_2,j_3,k_1,l+2k_2,k_3}, \qquad (6.13)$$

$$d^v_{j_1,j_2,j_3-1,k_1,k_2,k_3} = \sum_l g^{*0}_l c^v_{j_1,j_2,j_3,k_1,k_2,l+2k_3},$$

$$c^v_{j_1+1,j_2,j_3,k_1,k_2,k_3} = \sum_l (h^0_{k-2l} c^v_{j_1,j_2,j_3,l,k_2,k_3} + g^0_{k-2l} d^v_{j_1,j_2,j_3,l,k_2,k_3}),$$

$$c^v_{j_1,j_2+1,j_3,k_1,k_2,k_3} = \sum_l (h^1_{k-2l} c^v_{j_1,j_2,j_3,k_1,l,k_3} + g^1_{k-2l} d^v_{j_1,j_2,j_3,k_1,l,k_3}),$$

$$c^v_{j_1,j_2,j_3+1,k_1,k_2,k_3} = \sum_l (h^0_{k-2l} c^v_{j_1,j_2,j_3,k_1,k_2,l} + g^0_{k-2l} d^v_{j_1,j_2,j_3,k_1,k_2,l}).$$

$$c^w_{j_1-1,j_2,j_3,k_1,k_2,k_3} = \sum_l h^{*0}_l c^w_{j_1,j_2,j_3,l+2k_1,k_2,k_3},$$

$$c^w_{j_1,j_2-1,j_3,k_1,k_2,k_3} = \sum_l h^{*0}_l c^w_{j_1,j_2,j_3,k_1,l+2k_2,k_3},$$

$$c^w_{j_1,j_2,j_3-1,k_1,k_2,k_3} = \sum_l h^{*1}_l c^w_{j_1,j_2,j_3,k_1,k_2,l+2k_3},$$

$$d^w_{j_1-1,j_2,j_3,k_1,k_2,k_3} = \sum_l g^{*0}_l c^w_{j_1,j_2,j_3,l+2k_1,k_2,k_3},$$

$$d^w_{j_1,j_2-1,j_3,k_1,k_2,k_3} = \sum_l g^{*0}_l c^w_{j_1,j_2,j_3,k_1,l+2k_2,k_3}, \qquad (6.14)$$

$$d^w_{j_1,j_2,j_3-1,k_1,k_2,k_3} = \sum_l g^{*1}_l c^w_{j_1,j_2,j_3,k_1,k_2,l+2k_3},$$

$$c^w_{j_1+1,j_2,j_3,k_1,k_2,k_3} = \sum_l (h^0_{k-2l} c^w_{j_1,j_2,j_3,l,k_2,k_3} + g^0_{k-2l} d^w_{j_1,j_2,j_3,l,k_2,k_3}),$$

$$c^w_{j_1,j_2+1,j_3,k_1,k_2,k_3} = \sum_l (h^0_{k-2l} c^w_{j_1,j_2,j_3,k_1,l,k_3} + g^0_{k-2l} d^w_{j_1,j_2,j_3,k_1,l,k_3}),$$

$$c^w_{j_1,j_2,j_3+1,k_1,k_2,k_3} = \sum_l (h^1_{k-2l} c^w_{j_1,j_2,j_3,k_1,k_2,l} + g^1_{k-2l} d^w_{j_1,j_2,j_3,k_1,k_2,l}).$$

# 7. OPTIMIZATION ON QUOTIENT MANIFOLD

## 7.1 Representations of Quotient Manifold

Quotient manifold is an abstract manifold on which any given point is an equivalent class. Practically representation of this abstract manifold in original space need to found in order to conduct computation and optimization on it. Mathematical tools related to this topic have been developed in previous research (Absil et al. [2009], Huang [2013]). A brief introduction of these mathematical objects is offered here in order to regularize subsequent discussion. Use symbols $\mathcal{N}$, $\mathcal{Q}$, $h$, $m$ as declared in Chap. 4. Denote $\pi(h, m)$ as the mapping from $(h, m) \in \mathcal{N}$ to $[(h, m)] \in \mathcal{Q}$. Then $\pi^{-1}(\pi(h, m))$ represents a subset of $\mathcal{N}$ containing equivalent elements belonging to the same equivalent class. Denote $T_{(h,m)}\mathcal{N}$ as the tangent space of $\mathcal{N}$ at point $(h, m)$. For any tangent vector $\zeta_{(h,m)} \in T_{(h,m)}\mathcal{N}$, $\zeta_{(h,m)} = (\zeta_h, \zeta_m)$, where $\zeta_h \in \mathbb{C}^K$, $\zeta_h \in \mathbb{C}^N$ are two components of $\zeta_{(h,m)}$. Define vertical space $\mathbb{V}_{(h,m)}$ at a point $(h, m) \in \pi^{-1}(\pi(h, m))$ as the tangent space of $\pi^{-1}(\pi(h, m))$:

$$\mathbb{V}_{(h,m)} = \{(-h\Lambda, m\Lambda^*)|\Lambda \in \mathbb{C}\}. \tag{7.1}$$

Denote $g_{h,m}(\eta_{(h,m)}, \zeta_{(h,m)})$ as a Riemannian metric of $\mathcal{N}$. Then the horizontal space $\mathbb{H}_{(h,m)}$ can be defined as a subspace of $T_{(h,m)}\mathcal{N}$ that is orthogonal to $\mathbb{V}_{(h,m)}$ with respect to Riemannian metric $g_{(h,m)}$. In this research, a Riemannian metric as Huang and Hand [2017] is introduced for computational reasons:

$$g_{(h,m)}(\eta_{(h,m)}, \xi_{(h,m)}) = \text{Re}(\text{trace}(\eta_h^* \xi_h(m^*m) + \eta_h^* \xi_h(m^*m))). \tag{7.2}$$

The Riemannian metric $g_{(h,m)}(\eta_{(h,m)}, \xi_{(h,m)})$ of this form is chosen in this problem because it need to give the same value for different pairs of $(h, m)$ in the same equivalent class, which is a necessary condition for $g_{(h,m)}(\eta_{(h,m)}, \xi_{(h,m)})$ to induce a Riemannian

metric on $\mathcal{Q}$. Then the horizontal space $\mathbb{H}$ gives the following form (Huang and Hand [2017]):

$$\mathbb{H}_{(h,m)} = \left\{ \left( \begin{bmatrix} h & h_\perp \end{bmatrix} \begin{bmatrix} K \\ T \end{bmatrix}, \begin{bmatrix} m & m_\perp \end{bmatrix} \begin{bmatrix} K^* \\ Q \end{bmatrix} \right) | K \in \mathbb{C}, T \in \mathbb{C}^{K-1}, Q \in \mathbb{C}^{N-1} \right\}, \tag{7.3}$$

where $H_\perp$ is an orthonormal matrix with dimension $K \times (K-1)$ such that $H^* H_\perp = 0$, $M_\perp$ is an orthonormal matrix with dimension $N \times (N-1)$ such that $M^* M_\perp = 0$. The horizontal space $\mathbb{H}_{(h,m)}$ is found to be an equivalent representation of $T_{\pi(h,m)}\mathcal{Q}$ in $T_{\pi(h,m)}\mathcal{N}$. For any tangent vector $\eta_{\pi(h,m)} \in T_{\pi(h,m)}\mathcal{Q}$, there exists a unique vector $\eta_{\uparrow(h,m)} \in T_{\pi(h,m)}\mathcal{N}$ such that $D\pi(h,m)[\eta_{\uparrow(h,m)}] = \eta_{\pi(h,m)}$ (Absil et al. [2009]). $\eta_{\uparrow(h,m)}$ is called horizontal lift of $\eta_{\pi(h,m)}$. The following results about horizontal space and Riemannian metric are from Absil et al. [2009], Huang and Hand [2017], Huang [2013].

**Lemma 7.1.1.** *A vector field $(\hat{\theta}, \hat{\vartheta})$ on $\mathcal{N}$ is the horizontal lift of a vector field on $\mathcal{Q}$ if and only if, for each $(h, m) \in \mathcal{N}$, we have:*

$$(\hat{\theta}_{hp^{-1}}, \hat{\vartheta}_{mp^*}) = (\hat{\theta}_h p^{-1}, \hat{\vartheta}_m p^*), \tag{7.4}$$

*for all $p \in GL(1)$*

**Lemma 7.1.2.** *The following defines a Riemannian metric on $\mathcal{Q}$:*

$$g_{\pi(h,m)}(\eta_{\pi(h,m)}, \xi_{\pi(h,m)}) = \mathrm{Re}(\mathrm{trace}(\eta_{\uparrow h}^* \xi_{\uparrow h}(m^* m) + \eta_{\uparrow m}^* \xi_{\uparrow m}(h^* h))). \tag{7.5}$$

**Lemma 7.1.3.** *The orthogonal peojection to the vertical space $\mathbb{V}_{(h,m)}$ is $P_{(h,m)}^v(\eta_{(h,m)}) = (-h\Lambda, m\Lambda^*)$, where $\Lambda = \frac{1}{2}(\eta_m^* m(m^* m)^{-1} - (h^* h)^{-1} h^* \eta_h)$. The orthogonal projection to the horizontal space $\mathbb{H}_{(h,m)}$ is $P_{(h,m)}^h(\eta_{(h,m))} = \eta_{(h,m)} - P_{(h,m)}^v(\eta_{(h,m)})$.*

## 7.2 Retraction

Gradient decent optimization algorithms seek to minimize a cost function $f(x)$ on a manifold $\mathcal{M}$ along $\eta = -\mathrm{grad}f \in T_x\mathcal{M}$. Movement of a point $x$ along a tangent vector $\eta$ in a vector space (flat manifold) is trivial. For a general manifold with

arbitrary metric, $x$ might leave $\mathcal{M}$ after movement along $\eta$. Thus, retraction was introduced to move a point $x$ along certain direction meanwhile enforce $x$ to stay on $\mathcal{M}$. Definition and properties of retraction refer to multiple literature (e.g. Absil et al. [2009]):

**Definition 7.2.1.** *A retraction on a manifold $\mathcal{M}$ is a smooth mapping $R$ from the tangent bundle $T\mathcal{M}$ onto $\mathcal{M}$ satisfying the following properties. Let $R_x$ be the restriction of $R$ to $T_x\mathcal{M}$*

*(i)$R_x(0_x) = x$, where $0_x$ is the zero element in $T_x\mathcal{M}$.*

*(ii) With the canonical identification $T_{0_x}T_x\mathcal{M} \simeq T_x\mathcal{M}$, $R_x$ satisfies:*

$$\mathrm{D}R_x(0_x) = \mathrm{id}_{T_x\mathcal{M}}, \tag{7.6}$$

*where $\mathrm{id}_{T_x\mathcal{M}}$ is the identity mapping on $T_x\mathcal{M}$*

In the definition, 7.6 is the local rigidity condition, that is: locally $R_x(\eta_x) \in M$ will be on the direction $\eta_x$ with respect to $x$. A retraction in space $\mathcal{N}$ is as follow(Huang and Hand [2017]):

$$R_{(h,m)}(\eta_{(h,m)})H + \eta_H, M + \eta M). \tag{7.7}$$

Then a retraction on the quotient manifold $Q$ can be defined as follow:

$$\tilde{R}_{(h,m)}(\eta_{(h,m)}) = \pi(R_{(h,m)}(\eta_{\uparrow(h,m)})). \tag{7.8}$$

## 7.3 Riemannian Gradient

The concept of Riemannian gradient is introduced to give a direction of steepest decent on Riemannian Manifold. Given a scalar function $f$ on a Riemannian manifold $\mathcal{M}$, the Riemannian gradient $\mathrm{grad}f \in T_x\mathcal{M}$ of $f(x)$ is defined as the unique tangent vector satisfying:

$$\mathrm{D}f(x)[\eta_x] = g(\mathrm{grad}f(x), \eta_x), \forall \eta_x \in T_x\mathcal{M}, \tag{7.9}$$

where $\mathrm{D}f(x)[\eta_x]$ is the directional derivative of $f(x)$. Riemannian gradient $\mathrm{grad}f$ can be related to Euclidian gradient $\mathrm{grad}_e f$ (Absil et al. [2009]):

$$\mathrm{grad}f(x) = G^{-1}\,\mathrm{grad}_e f, \tag{7.10}$$

in which $G$ is the Riemannian metric matrix. The Riemannian gradient in this problem is as follow (Huang and Hand [2017]):

**Lemma 7.3.1.** *Given any $\pi(h, m) \in \mathcal{Q}$, the Riemannian gradient of $\tilde{f}_{\pi(h,m)}$ is*

$$(\operatorname{grad}\tilde{f}(\pi(h, m)))_{\uparrow(h,m)} = P^h_{(h,m)}(\nabla_h\tilde{f}(h, m)(m^*m)^{-1}, \nabla_m\tilde{f}(h, m)(h^*h)^{-1}), \quad (7.11)$$

*in which:*

$$\begin{aligned}
\nabla_h\tilde{f}(h, m) &= 2(B^*\operatorname{diag}(\operatorname{diag}(Bhm^*C^*) - y)C)m, \\
\nabla_m\tilde{f}(h, m) &= 2(B^*\operatorname{diag}(\operatorname{diag}(Bhm^*C^*) - y)C)^*h.
\end{aligned} \quad (7.12)$$

## 7.4  Riemannian Steepest Descent Algorithm

Steepest decent algorithm has been widely applied in optimization problems on Euclidian space (Boyd and Vandenberghe [2004]). An Riemannian steepest decent algorithm was introduced to solve optimization problems defined on Riemannian manifold with proper metric. The Riemannian steepest descent algorithm used here is stated in Table 7.1

Table 7.1.
Riemannian Steepest Descent Algorithm

1  $k = 0, h = h_0, m = m_0$.

2  for $k = 0, 1, 2, 3,$

3  Set $(h_{k+1}, m_{k+1}) = \tilde{R}_{h_k, m_k}(-\alpha(\operatorname{grad}\tilde{f}(\pi(h, m)))_{\uparrow(h,m)})$

4  End for

# 8. NUMERICAL RESULTS

## 8.1 Code Realization

The Divergence-Free Fast Wavelet Transform and Inverse Fast Wavelet Transform is implemented in Python for structured data. The Riemannian Manifold Optimization Library (ROPTLIB) is used to perform Riemannian Optimization (Huang et al. [2016]). A problem class for this 3D vector field deconvolution problem is written in C++ to call the ROPTLIB. A Python-C++ interface is written to enable Optimization code to call FWT functions. The matrix $B$ is the $L \times L$ DFT matrix. The matrix $W$ is the $L \times N$ 3-D FWT matrix.

## 8.2 Data Resource for Artificial Problem

DNS data of turbulent channel flow from John Hopkins Turbulence Database was used to generate and solve artificial problem of blind deconvolution (Li et al. [2008], Perlman et al. [2007], Graham et al. [2016]). A cube data with total number of grid points $N = 24^3$ and physical volume $V = 0.48^3$ in the boundary layer near the wall was downloaded as primary DNS data. An Gaussian filter of size $3^3$ was convoluted with the DNS data to form a filtered data set (artificial LES data).

## 8.3 Extension and Smoothing

The wavelet transform and MRA theory are applicable for functions defined on real line (or $\mathbb{R}^3$ for 3-D cases). For functions on an interval (or cube region in $\mathbb{R}^3$), the function is periodically extended to the whole space to apply wavelet transform. However, discontinuities appear when we try to periodically extend non-periodic functions. Similar to Fourier expansion, wavelet expansion of $f \in L^2$ lacks global convergence

properties, which leads to oscillation when encountered with discontinuities. Such Gibbs phenomenon of spline wavelets have been discussed in previous research (Shim and Volkmer [1996]). It can be observed that the deconvolution result of this problem oscillates drastically and gives no useful information(Fig. 8.1). An simple smoothing



(a) Original Velocity Field   (b) Filtered Velocity FIeld  (c)   Deconvoluted   Velocity Field
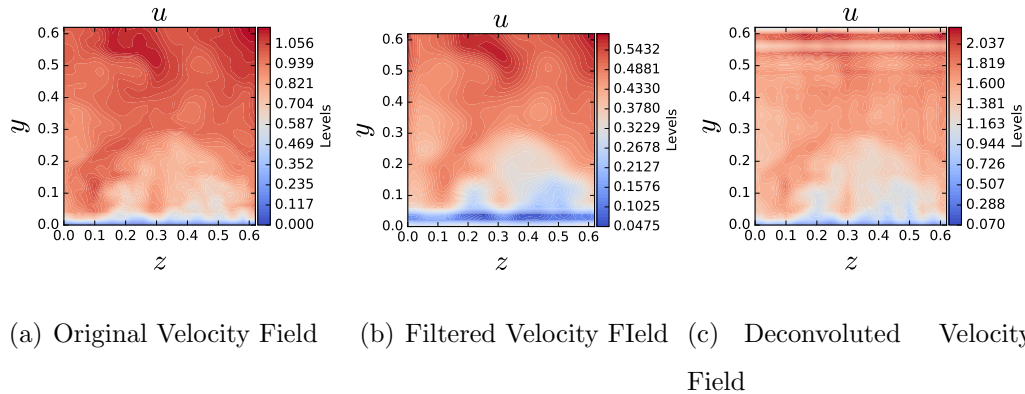
Figure 8.1.  Deconvolution without smoothing extension

extension is introduced to eliminate this oscillation(Fig. 8.2). Upper row of Fig. 8.2 is a series of non-periodic signal which is extended periodically. A drastic jump happens at the joints. In the lower row, a buffer layer is introduced into the signal and smoothly connects the beginning and end of the series. In this way, the oscillation can be largely eliminated and a reasonable solution is obtained. In this problem, the buffer layers are added on all three directions with smooth interpolation.

## 8.4   Deconvolution of Turbulent Boundary Layer

Deconvoluted velocity field are shown in Fig. 8.3, 8.4, 8.5, which is compared with original velocity field and filtered velocity field. This 2-D section is chosen to be the cross section of channel, the normal vector of this plane is on streamwise direction. It can be observed that local structures which are smoothed out by the Gaussian filter are successfully reconstructed on all three velocity components, especially for
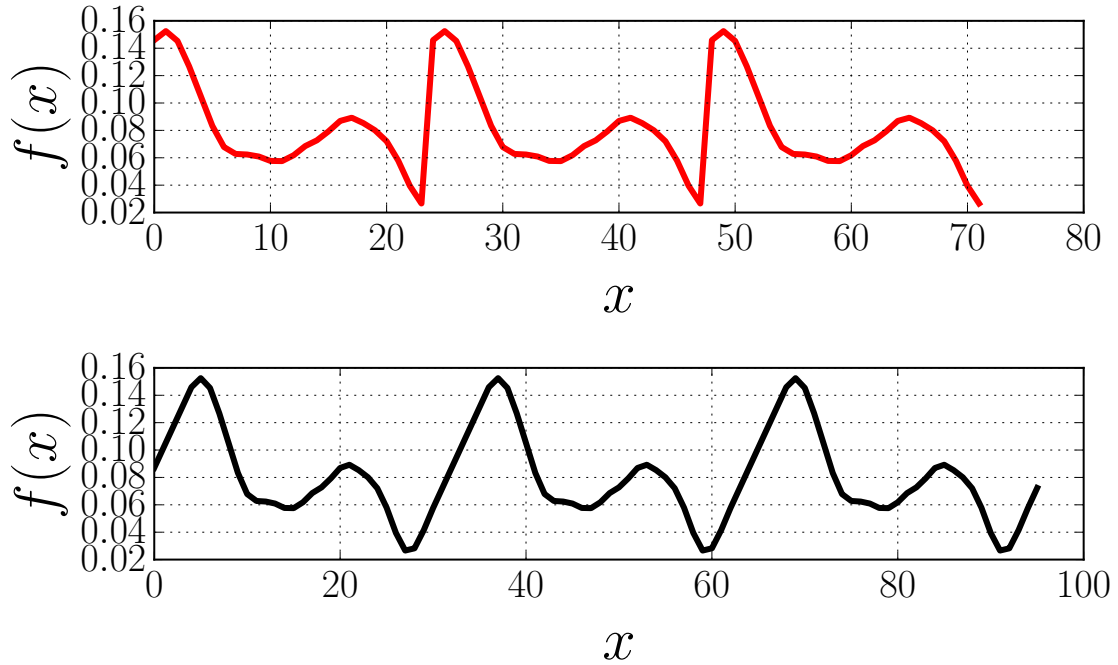
Figure 8.2.  Smoothing of periodically extended signal with jumps

complex structures in the boundary layer.  $L^2$ errors of filtered and deconvoluted velocity field are compared in Table 8.1.  The deconvoluted velocity components $u_d, v_d, w_d$ approximates the original velocity field $u, v, w$ very well compared with the filtered velocity $\tilde{u}, \tilde{v}, \tilde{w}$ in all three directions with respect to $L^2$ norm, which gives quantitative indication of deconvolution performance.

Table 8.1.

$L^2$ error of Reconstruction

| $\frac{\|u-\tilde{u}\|_2^2}{\|u\|_2^2}$ | $\frac{\|u-u_d\|_2^2}{\|u\|_2^2}$ | $\frac{\|v-\tilde{v}\|_2^2}{\|v\|_2^2}$ | $\frac{\|v-v_d\|_2^2}{\|v\|_2^2}$ | $\frac{\|w-\tilde{w}\|_2^2}{\|w\|_2^2}$ | $\frac{\|w-w_d\|_2^2}{\|w\|_2^2}$ |
|---|---|---|---|---|---|
| 0.4238 | 0.0756 | 0.5425 | 0.0645 | 0.4603 | 0.0777 |

(a) Original Velocity Field    (b) Filtered Velocity Field    (c)   Deconvoluted   Velocity Field
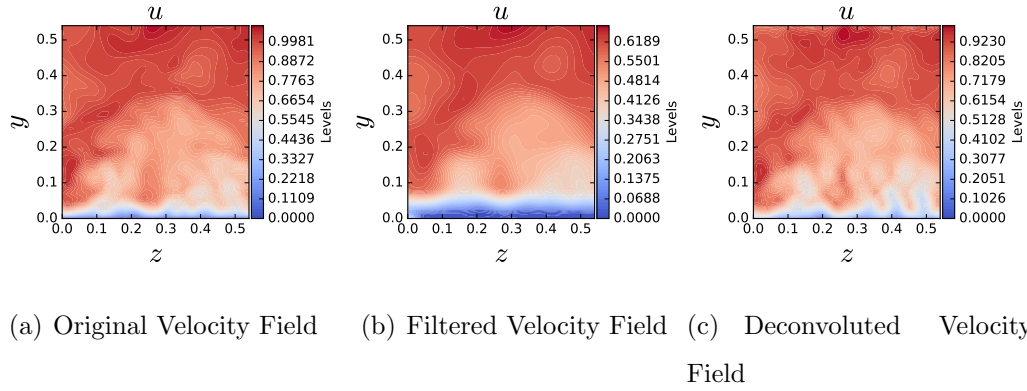
Figure 8.3.   Deconvolution results of $u$



(a) Original Velocity Field    (b) Filtered Velocity Field    (c)   Deconvoluted   Velocity Field
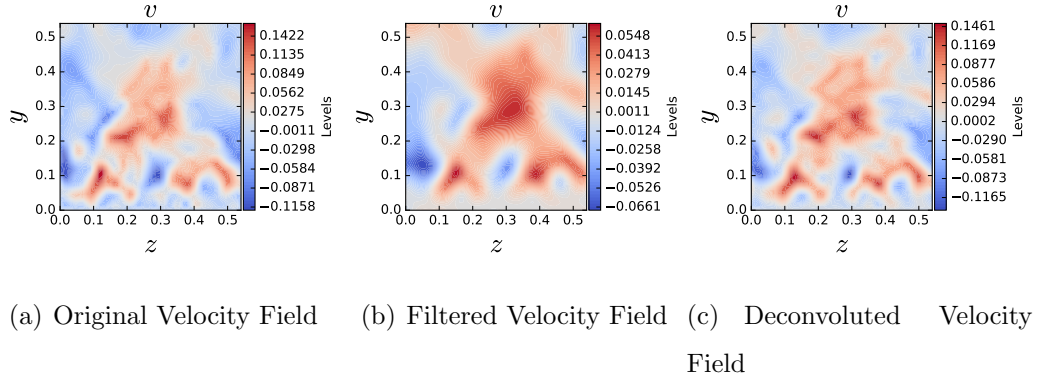
Figure 8.4.   Deconvolution result of $v$



(a) Original Velocity Field    (b) Filtered Velocity Field    (c)   Deconvoluted   Velocity Field
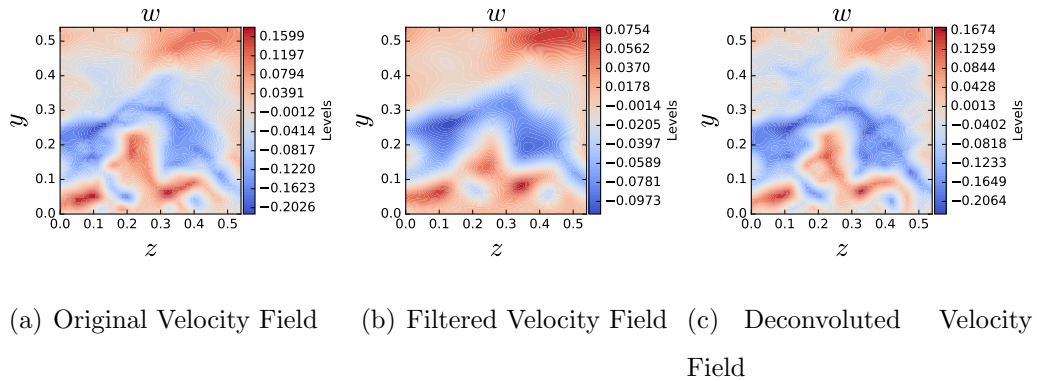
Figure 8.5.   Deconvolution result of $w$

# Part IV

# Conclusion and Discussion

## 9. CONCLUSION

In Part II, a new method of turbulence generation was proposed and evaluated in both the homogeneous and inhomogeneous turbulence cases. Various properties of the generated isotropic homogeneous turbulence show good agreement with both the input data and the theoretical results, including spatial, spectral and frequency properties. The generated fully developed channel flow shows desired spectral and spatial characteristics for different wavenumbers. Preservation of Reynolds stress for this method is verified through both theoretical deduction and numerical simulation.

Comparison of characteristics of the Stochastic Wavelet Method and SRFM in homogeneous and inhomogeneous turbulence synthesis is listed in Tab. 9.1. The number of modes of different wavenumbers used in turbulence synthesis with Stochastic Wavelet Model is far smaller than that required by SRFM. Also, this new method could fully preserve normal Reynolds stress as well as incompressibility in inhomogeneous and anisotropic turbulence, which could not be achieved with SRFM. Moreover, the computational cost of the Stochastic Wavelet Model could be largely reduced without much loss of the turbulent kinetic energy, leading to far less computation cost in comparison with SRFM.

| | Homogeneous | | Inhomogeneous | | | |
|------|---------|-------------|----------|------------------|-------------------|-------------|
| | $Re_L$ | Mode Number | $Re_\tau$ | Reynolds Stress | Incompressibility | Mode Number |
| SFRM | 723 | 5000 | 400 | Preserved | Not Preserved | 500 - 5000 |
| SWM | 4206 | 10-20 | 141900 | Preserved | Preserved | 15-30 |

Table 9.1.
Comparison of SFRM and Stochastic Wavelet Model simulation results.

In Part III, a framework of turbulence deconvolution was developed and tested with artificial problem. The blind deconvolution problem is transformed into an optimization problem on a quotient manifold, which is further equipped with a Riemannian metric and turned into Riemannian manifold. The optimization problem is solved using the Riemannian steepest descent algorithm. Divergence-Free Wavelet is introduced to preserve mass conservation during optimization process and to reduce computational cost. The deconvolution algorithm performs well both quantitatively and qualitatively.

Compared to previous research related to turbulence deconvolution, there are multiple remarkable improvements in this research. This is the first work to directly deconvolute turbulent boundary layer without any prior knowledge of spectral and structural properties of boundary layer which is commonly needed for reconstruction. This is also the first work to introduce Riemannian optimization techniques into turbulence related problems. This work generally could preserves divergence-free condition through the deconvolution process, which was barely achieved in previous research, especially in inhomogeneous anisotropic turbulence.

## 10. FUTURE PERSPECTIVES

Stochastic Wavelet Method issued in Part II exhibits great potential in both scientific computing research and industrial application. Effective and low-cost inlet boundary generation is important for high-fidelity turbulence simulation (DNS, LES) and has become an important research topic recently. In addition, the interface between the RANS region and the LES region in zonal Detached Eddy Simulation also requires turbulence synthesis from RANS data. The Stochastic Wavelet Method proposed in Part II provides a new approach to synthesize turbulence fluctuation fields with desired spectral and statistical properties other than which are not attainable using traditional SRFM under divergence-free constraint. Also, this method could further be applied to computer graphics and the movie industry to generate realistic fluid flows in animations with very low computation cost.

There are several key points that need to be considered for the further development of the framework proposed in Part III. Although $\mathbb{L}^2$ norm of the error of deconvolution result has been computed as an indication of recover accuracy, it is still not clear how much physics is recovered from the computation. Thus further computation of statistics of deconvoluted result need to be conducted to exam its effect on flow structures. Also, artificial problems with different types of filter need to be solved in order to evaluate the influence of filter type on the process of deconvolution. It is still not clear about the minimum information required to fully recover the exact distribution of velocity field. There should be a correlation between minimum information of velocity field (determined by local Reynolds number and filter width) and possibility of exact deconvolution, below which this problem becomes ill-defined and could not be solved. Also, in real Large Eddy Simulation, errors are introduced by subgrid stress models. It becomes important to study the behavior of this framework when the input filtered field is polluted with error, especially non-Gaussian errors.

REFERENCES

# REFERENCES

P-A Absil, Robert Mahony, and Rodolphe Sepulchre. *Optimization algorithms on matrix manifolds*. Princeton University Press, 2009.

GR Ayers and J Christopher Dainty. Iterative blind deconvolution method and its applications. *Optics letters*, 13(7):547–549, 1988.

Mattias Billson, Lars-Erik Eriksson, and Lars Davidson. Jet noise prediction using stochastic turbulence modeling. In *9th AIAA/CEAS Aeroacoustics Conference and Exhibit*, page 3282, 2003.

Stephen Boyd and Lieven Vandenberghe. *Convex optimization*. Cambridge university press, 2004.

Robert Bridson, Jim Houriham, and Marcus Nordenstam. Curl-noise for procedural fluid flow. *ACM Transactions on Graphics (TOG)*, 26(3):46, 2007.

Hugo G Castro and Rodrigo R Paz. A time and space correlated turbulence synthesis method for large eddy simulations. *Journal of Computational Physics*, 235:742–763, 2013.

Robert L Cook and Tony DeRose. Wavelet noise. *ACM Transactions on Graphics (TOG)*, 24(3):803–811, 2005 2005.

Ingrid Daubechies. *Ten lectures on wavelets*. SIAM, 1992.

Erwan Deriaz and Valérie Perrier. Towards a divergence-free wavelet method for the simulation of 2d/3d turbulent flows. *J. Turbul*, 7(3), 2005.

Erwan Deriaz and Valérie Perrier. Divergence-free and curl-free wavelets in two dimensions and three dimensions: application to turbulent flows. *Journal of Turbulence*, (7):N3, 2006.

Erwan Deriaz and Valérie Perrier. Orthogonal helmholtz decomposition in arbitrary dimension using divergence-free and curl-free wavelets. *Applied and Computational Harmonic Analysis*, 26(2):249–269, 2009.

J Andrzej Domaradzki and Kuo-Chieh Loh. The subgrid-scale estimation model in the physical space representation. *Physics of Fluids*, 11(8):2330–2342, 1999.

Marie Farge. Wavelet transforms and their applications to turbulence. *Annual review of fluid mechanics*, 24(1):395–458, 1992.

Marie Farge and Kai Schneider. Coherent vortex simulation (cvs), a semi-deterministic turbulence model using wavelets. *Flow, Turbulence and Combustion*, 66(4):393–426, 2001.

Jimmy Chi Hung Fung, Julian CR Hunt, NA Malik, and RJ Perkins. Kinematic simulation of homogeneous turbulence by unsteady random fourier modes. *Journal of Fluid Mechanics*, 236:281–318, 1992.

Aditya S Ghate and Sanjiva K Lele. Subfilter-scale enrichment of planetary boundary layer large eddy simulation using discrete fourier–gabor modes. *Journal of Fluid Mechanics*, 819:494–539, 2017.

Jonas Gomes and Luiz Velho. *From fourier analysis to wavelets*. 2015.

J Graham, K Kanov, XIA Yang, M Lee, N Malaya, CC Lalescu, R Burns, G Eyink, A Szalay, RD Moser, et al. A web services accessible database of turbulent channel flow and its use for testing a new integral wall model for les. *Journal of Turbulence*, 17(2):181–215, 2016.

Guowei He, Guodong Jin, and Yue Yang. Space-time correlations and dynamic coupling in turbulent flows. *Annual Review of Fluid Mechanics*, 49:51–70, 2017.

Eugenio Hernández and Guido Weiss. *A first course on wavelets*. CRC press, 1996.

SH Huang, QS Li, and JR Wu. A general inflow turbulence generator for large eddy simulation. *Journal of Wind Engineering and Industrial Aerodynamics*, 98 (10):600–617, 2010.

Wen Huang. *Optimization algorithms on Riemannian manifolds with applications*. PhD thesis, The Florida State University, 2013.

Wen Huang and Paul Hand. Blind deconvolution by a steepest descent algorithm on a quotient manifold. *arXiv preprint arXiv:1710.03309*, 2017.

Wen Huang, PA Absil, KA Gallivan, and Paul Hand. Roptlib: an object-oriented c++ library for optimization on riemannian manifolds. Technical report, Florida State University, 2016.

Takashi Ishihara, Toshiyuki Gotoh, and Yukio Kaneda. Study of high–reynolds number isotropic turbulence by direct numerical simulation. *Annual Review of Fluid Mechanics*, 41:165–180, 2009.

N. Jarrin, R. Prosser, J.-C. Uribe, S. Benhamadouche, and D. Laurence. Reconstruction of turbulent fluctuations for hybrid rans/les simulations using a synthetic-eddy method. *International Journal of Heat and Fluid Flow*, 30(3):435 – 442, 2009. The Seventh International Symposium on Engineering Turbulence Modelling and Measurements, ETMM7.

Christophe Baillytand Daniel Juves. A stochastic approach to compute subsonic-noise using linearized euler's equations. *AIAA journal*, 1999.

Jean-Pierre Kahane, Pierre Gilles Lemarié, and Pierre-Gilles Lemarié-Rieusset. *Fourier series and wavelets*, volume 3. Routledge, 1995.

Yukio Kaneda, Takashi Ishihara, Mitsuo Yokokawa, Ken'ichi Itakura, and Atsuya Uno. Energy dissipation rate and energy spectrum in high resolution direct numerical simulations of turbulence in a periodic box. *Physics of Fluids*, 15(2):L21–L24, 2003.

Aggelos K Katsaggelos and Kuen-Tsair Lay. Maximum likelihood blur identification and image restoration using the em algorithm. *IEEE Transactions on Signal Processing*, 39(3):729–733, 1991.

Theodore Kim, Nils Thürey, Doug James, and Markus Gross. Wavelet turbulence for fluid simulation. In *ACM Transactions on Graphics (TOG)*, volume 27, page 50. ACM, 2008.

Andrey Nikolaevich Kolmogorov. The local structure of turbulence in incompressible viscous fluid for very large reynolds numbers. In *Dokl. Akad. Nauk SSSR*, volume 30, pages 299–303, 1941.

Robert H Kraichnan. Diffusion by a random velocity field. *The physics of fluids*, 13 (1):22–31, 1970.

Deepa Kundur and Dimitrios Hatzinakos. Blind image deconvolution. 13(3):43–64, 1996.

Anthony Lafitte, Thomas Le Garrec, Christophe Bailly, and Estelle Laurendeau. Turbulence generation from a sweeping-based stochastic model. *AIAA journal*, 52 (2):281–292, 2014.

Hung Le, Parviz Moin, and John Kim. Direct numerical simulation of turbulent flow over a backward-facing step. *Journal of fluid mechanics*, 330:349–374, 1997.

DC Leslie and Cecil E Leith. Developments in the theory of turbulence. *Physics Today*, 28:59, 1975.

Anat Levin, Yair Weiss, Fredo Durand, and William T Freeman. Understanding and evaluating blind deconvolution algorithms. In *Computer Vision and Pattern Recognition, 2009. CVPR 2009. IEEE Conference on*, pages 1964–1971. IEEE, 2009.

Yi Li, Eric Perlman, Minping Wan, Yunke Yang, Charles Meneveau, Randal Burns, Shiyi Chen, Alexander Szalay, and Gregory Eyink. A public turbulence database cluster and applications to study lagrangian evolution of velocity increments in turbulence. *Journal of Turbulence*, (9):N31, 2008.

Thomas S Lund, Xiaohua Wu, and Kyle D Squires. Generation of turbulent inflow data for spatially-developing boundary layer simulations. *Journal of Computational Physics*, 140(2):233–258, 1998.

Stéphane Mallat. *A wavelet tour of signal processing.* 1999.

Charles Meneveau. Analysis of turbulence in the orthonormal wavelet representation. *Journal of Fluid Mechanics*, 232:469–520, 1991.

Parviz Moin and Krishnan Mahesh. Direct numerical simulation: a tool in turbulence research. *Annual review of fluid mechanics*, 30(1):539–578, 1998.

Ken Perlin. An image synthesizer. *ACM Siggraph Computer Graphics*, 19(3):287–296, 1985.

Eric Perlman, Randal Burns, Yi Li, and Charles Meneveau. Data exploration of turbulence simulations using a database cluster. In *Proceedings of the 2007 ACM/IEEE conference on Supercomputing*, page 23. ACM, 2007.

Valérie Perrier, Thierry Philipovitch, and Claude Basdevant. Wavelet spectra compared to fourier spectra. *Journal of Mathematical Physics*, 36(3):1506–1519, 1995.

R Poletto, T Craft, and A Revell. A new divergence free synthetic eddy method for the reproduction of inlet flow conditions for les. *Flow, turbulence and combustion*, 91(3):519–539, 2013.

Stephen B Pope. *Turbulent flows*. IOP Publishing, 2001.

Robert S Rogallo and Parviz Moin. Numerical simulation of turbulent flows. *Annual review of fluid mechanics*, 16(1):99–137, 1984.

Tony Saad, Derek Cline, Rob Stoll, and James C Sutherland. Scalable tools for generating synthetic isotropic turbulence with arbitrary spectra. *AIAA Journal*, 2016.

Pierre Sagaut, Sebastien Deck, and Marc Terracol. *Multiscale and multiresolution approaches in turbulence: LES, DES and hybrid RANS/LES methods: applications and guidelines*. World Scientific, 2013.

A Scotti and C Meneveau. A fractal model for large eddy simulation of turbulent flow. *Physica D: Nonlinear Phenomena*, 127(3):198–232, 1999.

Hong-Tae Shim and Hans Volkmer. On the gibbs phenomenon for wavelet expansions. *Journal of approximation theory*, 84(1):74–95, 1996.

Michael L Shur, Philippe R Spalart, Michael K Strelets, and Andrey K Travin. Synthetic turbulence generators for rans-les interfaces in zonal simulations of aerodynamic and aeroacoustic problems. *Flow, turbulence and combustion*, 93(1):63–92, 2014.

A Smirnov, S Shi, and I Celik. Random flow generation technique for large eddy simulations and particle-dynamics modeling. *Transactions of the ASME-I-Journal of Fluids Engineering*, 123(2):359–371, 2001.

Philippe R Spalart. Detached-eddy simulation. *Annual review of fluid mechanics*, 41:181–202, 2009.

John Stuelpnagel. On the parametrization of the three-dimensional rotation group. *SIAM review*, 6(4):422–430, 1964.

Karsten Urban. *Wavelets in numerical simulation: problem adapted construction and applications*, volume 22. Springer Science & Business Media, 2012.

Xiaohua Wu. Inflow turbulence generation methods. *Annual Review of Fluid Mechanics*, 49:23–49, 2017.

Rixin Yu and Xue-Song Bai. A fully divergence-free method for generation of inhomogeneous and anisotropic turbulence with large spatial variation. *Journal of Computational Physics*, 256:234–253, 2014.

APPENDIX

## A. PROOF OF REYNOLDS STRESS PRESERVATION

Consider turbulence field in a finite domain $\Omega$ of size $|\Omega|$. To prove the preservation of Reynolds stress tensor in scheme Eq.(2.1), (2.2), (2.3), first to prove $\boldsymbol{v} = \nabla \times \boldsymbol{M}$ satisfies:

$$\langle \boldsymbol{v}\boldsymbol{v} \rangle = \underline{\underline{I}}.$$

Proof:

$$\boldsymbol{v} = \nabla \times \sum_{|\boldsymbol{k}| \in K} \sum_{\boldsymbol{x}_p}^{N_i} q_{\boldsymbol{x}_p,\boldsymbol{k}} \boldsymbol{O}_{\boldsymbol{x}_p,\boldsymbol{k}}(\omega_{\boldsymbol{x}_p,\boldsymbol{k}} \Psi_{\boldsymbol{k}}(\boldsymbol{x} - \boldsymbol{x}_p)).$$

Curl is a linear operator and is invariant under rotation:

$$\boldsymbol{v} = \sum_{|\boldsymbol{k}| \in K} \sum_{\boldsymbol{x}_p}^{N_i} q_{\boldsymbol{x}_p,\boldsymbol{k}} \boldsymbol{O}_{\boldsymbol{x}_p,\boldsymbol{k}}(\nabla \times (\omega_{\boldsymbol{x}_p,\boldsymbol{k}} \Psi_{\boldsymbol{k}}(\boldsymbol{x} - \boldsymbol{x}_p))).$$

Rewrite into index form:

$$v_i = \sum_{|\boldsymbol{k}| \in K} \sum_{\boldsymbol{x}_p}^{N_i} q_{\boldsymbol{x}_p,\boldsymbol{k}} (\boldsymbol{O}_{\boldsymbol{x}_p,\boldsymbol{k}})_{il} \epsilon_{lmn} \partial_m (\omega_{\boldsymbol{x}_p,\boldsymbol{k}} \Psi_{\boldsymbol{k}}(\boldsymbol{x} - \boldsymbol{x}_p))_n$$

$$= \sum_{|\boldsymbol{k}| \in K} \sum_{\boldsymbol{x}_p}^{N_i} q_{\boldsymbol{x}_p,\boldsymbol{k}} (\boldsymbol{O}_{\boldsymbol{x}_p,\boldsymbol{k}})_{il} \epsilon_{lmn} (\omega_{\boldsymbol{x}_p,\boldsymbol{k}})_n \partial_m \Psi_{\boldsymbol{k}}(\boldsymbol{x} - \boldsymbol{x}_p).$$

$$\langle v_i v_j \rangle = \Big\langle \sum_{|\boldsymbol{k}_1| \in K} \sum_{\boldsymbol{x}_{p1}} \sum_{|\boldsymbol{k}_2| \in K}^{N_i} \sum_{\boldsymbol{x}_{p2}}^{N_i} q_{\boldsymbol{x}_{p1},\boldsymbol{k}_1} q_{\boldsymbol{x}_{p2},\boldsymbol{k}_2} (\boldsymbol{O}_{\boldsymbol{x}_{p1},\boldsymbol{k}_1})_{il} (\boldsymbol{O}_{\boldsymbol{x}_{p2},\boldsymbol{k}_2})_{jr}$$

$$\epsilon_{lmn} \epsilon_{rst} (\omega_{\boldsymbol{x}_{p1},\boldsymbol{k}_1})_n (\omega_{\boldsymbol{x}_{p2},\boldsymbol{k}_2})_t \partial_m \Psi_{\boldsymbol{k}_1}(\boldsymbol{x} - \boldsymbol{x}_{p1}) \partial_s \Psi_{\boldsymbol{k}_2}(\boldsymbol{x} - \boldsymbol{x}_{p2}) \Big\rangle$$

$$= \sum_{|\boldsymbol{k}_1| \in K} \sum_{\boldsymbol{x}_{p1}} \sum_{|\boldsymbol{k}_2| \in K}^{N_i} \sum_{\boldsymbol{x}_{p2}}^{N_i} q_{\boldsymbol{x}_{p1},\boldsymbol{k}_1} q_{\boldsymbol{x}_{p2},\boldsymbol{k}_2} \langle (\boldsymbol{O}_{\boldsymbol{x}_{p1},\boldsymbol{k}_1})_{il} (\boldsymbol{O}_{\boldsymbol{x}_{p2},\boldsymbol{k}_2})_{jr} \rangle$$

$$\epsilon_{lmn} \epsilon_{rst} \langle (\omega_{\boldsymbol{x}_{p1},\boldsymbol{k}_1})_n (\omega_{\boldsymbol{x}_{p2},\boldsymbol{k}_2})_t \rangle \langle \partial_m \Psi_{\boldsymbol{k}_1}(\boldsymbol{x} - \boldsymbol{x}_{p1}) \partial_s \Psi_{\boldsymbol{k}_2}(\boldsymbol{x} - \boldsymbol{x}_{p2}) \rangle.$$

For $p_1 \neq p_2$ or $k_1 \neq k_2$, $\langle (\omega_{\boldsymbol{x}_{p1},\boldsymbol{k}_1})_n (\omega_{\boldsymbol{x}_{p2},\boldsymbol{k}_2})_t \rangle = 0$. Therefore:

$$\langle v_i v_j \rangle = \sum_{|\boldsymbol{k}| \in K} \sum_{\boldsymbol{x}_p}^{N_i} q_{\boldsymbol{x}_p,\boldsymbol{k}}^2 \langle (\boldsymbol{O}_{\boldsymbol{x}_p,\boldsymbol{k}})_{il} (\boldsymbol{O}_{\boldsymbol{x}_p,\boldsymbol{k}})_{jr} \rangle \epsilon_{lmn} \epsilon_{rst}$$

$$\langle (\omega_{\bm{x}_p,\bm{k}})_n (\omega_{\bm{x}_p,\bm{k}})_t \rangle \langle \partial_m \Psi_{\bm{k}}(\bm{x} - \bm{x}_p) \partial_s \Psi_{\bm{k}}(\bm{x} - \bm{x}_p) \rangle.$$

$\bm{x}_p$ is uniformly distributed in the flow domain, thus the following hold:

$$\langle \partial_m \Psi_{\bm{k}}(\bm{x} - \bm{x}_p) \partial_s \Psi_{\bm{k}}(\bm{x} - \bm{x}_p) \rangle = \Big\langle \int_\Omega \partial_m \Psi_{\bm{k}} \partial_s \Psi_{\bm{k}} \, \mathrm{d}\bm{x} \Big\rangle.$$

From construction process in Eq.(2.7), $\partial_s \Psi_{\bm{k}}$ is symmetric along three axis, thus:

$$\Big\langle \int_\Omega \partial_m \Psi_{\bm{k}} \partial_s \Psi_{\bm{k}} \, \mathrm{d}\bm{x} \Big\rangle = \frac{c_k}{N_i} \delta_{ms},$$

where $c_k$ is defined in Eq.(2.12). Also notice $\langle (\omega_{\bm{x}_p,\bm{k}})_n (\omega_{\bm{x}_p,\bm{k}})_t \rangle = \delta_{nt}$. Plug into the expression of $\langle v_i v_j \rangle$:

$$\langle v_i v_j \rangle = \sum_{|\bm{k}| \in K} \sum_{\bm{x}_p}^{N_i} q_{\bm{x}_p,\bm{k}}^2 \langle (\bm{O}_{\bm{x}_p,\bm{k}})_{il} (\bm{O}_{\bm{x}_p,\bm{k}})_{jr} \rangle \epsilon_{lmn} \epsilon_{rst} \delta_{nt} \delta_{ms} \frac{c_k}{N_i}$$

$$= \sum_{|\bm{k}| \in K} \sum_{\bm{x}_p}^{N_i} 2 q_{\bm{x}_p,\bm{k}}^2 \langle (\bm{O}_{\bm{x}_p,\bm{k}})_{il} (\bm{O}_{\bm{x}_p,\bm{k}})_{jr} \rangle \delta_{lr} \frac{c_k}{N_i}$$

$$= \sum_{|\bm{k}| \in K} \sum_{\bm{x}_p}^{N_i} 2 q_{\bm{x}_p,\bm{k}}^2 \langle (\bm{O}_{\bm{x}_p,\bm{k}})_{il} (\bm{O}_{\bm{x}_p,\bm{k}})_{jl} \rangle \frac{c_k}{N_i}$$

$$= \sum_{|\bm{k}| \in K} \sum_{\bm{x}_p}^{N_i} 2 q_{\bm{x}_p,\bm{k}}^2 \delta_{ij} \frac{c_k}{N_i}$$

$$= \delta_{ij} \sum_{|\bm{k}| \in K} \frac{E(l) \Delta l}{2 k_t} \to \delta_{ij},$$

as $\Delta l \to 0, l_{max} \to \infty, l_{min} \to 0$. Thus for enough large $K$, the following hold:

$$\langle \bm{v} \bm{v} \rangle = \bm{I}.$$

Then:

$$\langle \bm{u} \bm{u} \rangle = \langle (\bm{A} \bm{v})(\bm{A} \bm{v}) \rangle,$$

$$= \bm{A}(\bm{v} \bm{v}) \bm{A}^T,$$

$$= \bm{A} \bm{A}^T = \bm{R}.$$

## B. WAVELET FUNCTIONS AND SCALING SEQUENCES

Wavelet functions used in III for divergence-free wavelet construction are spline wavelets of first and second order. B.1 and B.2 shows scaling sequences of $(V_j^0)_{j\in\mathbb{Z}}$ and $(V_j^1)_{j\in\mathbb{Z}}$.

Table B.1.

scaling sequence of $\phi^0$ and $\psi^0$

| $l$ | -2 | -1 | 0 | 1 | 2 | 3 |
|---|---|---|---|---|---|---|
| $\frac{1}{\sqrt{2}h_l^{*0}}$ | $-\frac{1}{8}$ | $\frac{1}{4}$ | $\frac{3}{4}$ | $\frac{1}{4}$ | $-\frac{1}{8}$ | 0 |
| $\frac{1}{\sqrt{2}g_l^{*0}}$ | 0 | 0 | $-\frac{1}{4}$ | $\frac{1}{2}$ | $-\frac{1}{4}$ | 0 |
| $\frac{1}{\sqrt{2}h_l^0}$ | 0 | $\frac{1}{4}$ | $\frac{1}{2}$ | $\frac{1}{4}$ | 0 | 0 |
| $\frac{1}{\sqrt{2}g_l^0}$ | 0 | $-\frac{1}{8}$ | $-\frac{1}{4}$ | $\frac{3}{4}$ | $-\frac{1}{4}$ | $-\frac{1}{8}$ |

Table B.2.

scaling sequence of $\phi^1$ and $\psi^1$

| $l$ | -1 | 0 | 1 | 2 |
|---|---|---|---|---|
| $\frac{1}{\sqrt{2}h_l^{*1}}$ | $-\frac{1}{4}$ | $\frac{3}{4}$ | $\frac{3}{4}$ | $-\frac{1}{4}$ |
| $\frac{1}{\sqrt{2}g_l^{*1}}$ | $\frac{1}{8}$ | $-\frac{3}{8}$ | $\frac{3}{8}$ | $-\frac{1}{8}$ |
| $\frac{1}{\sqrt{2}h_l^1}$ | $\frac{1}{8}$ | $\frac{3}{8}$ | $\frac{3}{8}$ | $\frac{1}{8}$ |
| $\frac{1}{\sqrt{2}g_l^1}$ | $-\frac{1}{4}$ | $-\frac{3}{4}$ | $\frac{33}{4}$ | $\frac{1}{4}$ |